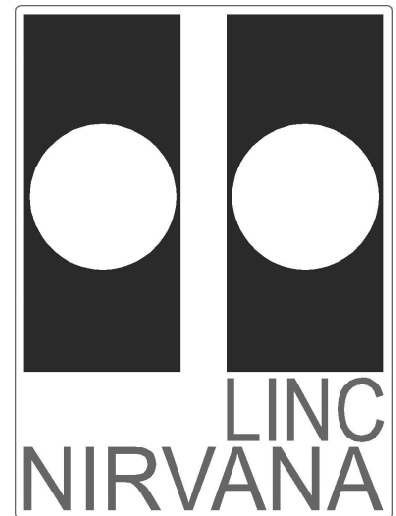


LINC-NIRVANA

The **L**BT **I**nterferometric **C**amera and
Near-**I**nfra**R**ed / **V**isible **A**daptive
interferometer for **A**stronomy

A collaborative project of the MPIA Heidelberg, INAF-Arcetri,
Universität zu Köln, and MPIfR Bonn

<http://www.mpia.de/LINC>



LINC-NIRVANA

Simulation studies with AIRY

Doc. No. LN-GENOVA-FDR-ASW-002
Short Title Simulation studies
Issue 1.0
Date 22 May 2005

Prepared	M. Bertero	22 May 2005	
	Name	Date	Signature
Approved	T. Driebe	22 May 2005	
	Name	Date	Signature
Released	M. Kürster	22 May, 2005	
	Name	Date	Signature

Document Change Record

Issue	Date	Section/Paragraph Affected	Reasons / Remarks
0.1	28 July 2004	all	First version
0.2	21 October 2004	all	Major improvements of all Sections. Addition of a Section on the simulation of a star cluster.
0.3	8 March 2005	all	Revision as required by the chapter editor
1.0	22 May 2005	All Sections	Modifications based on approver's comments

Contents

1	Scope	1
2	Authors	1
3	Applicable Documents	1
4	Acronyms and Abbreviations	1
5	References	2
6	Introduction	3
7	The model of image formation	4
8	The image deconvolution method	5
9	Resolution of binary systems	8
9.1	The interferometric PSFs and other parameters	8
9.2	Intrinsic limits in the restoration of the parameters of binary stars	8
10	Reconstruction of diffuse objects	9
11	Analysis of a simulated star cluster	11
12	Partial angular coverage and angular smearing	12
12.1	Discussion	16
13	Partial (and space-variant) Adaptive Optics correction	16
13.1	Space-variance of the AO-corrected PSF	17
13.2	Global AO-correction quality	19
13.3	Discussion	20
14	An example of a two-step method: resolution enhancement	21
15	Single-image approaches	23
16	Concluding remarks	31

List of Figures

1	Examples of PSFs and OTFs	3
2	Objects used for numerical experiments	7
3	Restoration of binary parameters	10
4	Reconstruction of a diffuse object	11
5	Reconstruction of the averaged power spectrum	11
6	Reconstruction of a star cluster	12
7	Reconstruction of <i>GG Tau</i> -like object	14
8	PSFs with and without smearing	15
9	Restoration errors for the <i>GG Tau</i> -like object	16

10	Wavefront residuals and corresponding interferometric image	18
11	Effect of the AO-correction on the reconstruction error	18
12	Reconstruction of the magnitude difference for different AO-correction levels	19
13	Reconstruction of a diffuse object for different AO-correction levels	20
14	Reconstruction errors in the case of uniform AO-correction	21
15	Example of resolution enhancement	22
16	OTFs of the single-image approaches	24
17	The AO-corrected PSFs used for the simulations described in Section 14	26
18	Example of reconstruction of a binary system	29
19	Behaviour of the flux of the binary object - Ideal PSFs	30
20	Behaviour of the flux of the binary object - AO-corrected PSFs	30
21	Behaviour of the flux of the binary object - AO-corrected PSFs with smearing effect	30

List of Tables

1	Observation parameters as functions of the object declination	13
2	Parameters of the AO-correction	19
3	Comparison between single-image and multi-image methods	27
4	Comparison between single-image and multi-image methods in the case of ideal PSFs	28
5	Comparison between single-image and multi-image methods in the case of AO-corrected PSFs	28
6	Comparison between single-image and multi-image methods in the case of AO-corrected PSFs with angular smearing effect	28

1 Scope

This document is a summary of the simulation studies performed with the software package AIRY. The purpose is to investigate the imaging and resolution capabilities of LINC-NIRVANA. In general, observations in the K-band are assumed and images are sampled at a rate consistent with, even if not identical to, the actual sampling rate of the LINC-NIRVANA detector.

2 Authors

This document has been written by Barbara Anconelli, Mario Bertero, Patrizia Boccacci, Gabriele Desiderá (DISI-Università di Genova), and Marcel Carbillet (LUAN-Université de Nice, formerly with Osservatorio Astrofisico di Arcetri).

3 Applicable Documents

No.	Title	Number and issue
1	AIRY Package	LN-GENOVA-FDR-ASW-001 [0.3]
2	Data Reduction Software	LN-MPIFR-FDR-ASW-001 [0.3]

4 Acronyms and Abbreviations

ADN	ADd Noise module of AIRY
AIRY	Astronomical Image Reconstruction in interferometrY
CAOS	Code for Adaptive Optics Simulation
CMD	Color-Magnitude Diagram
CNV	CoNVolution module of AIRY
DEC	DEConvolution module of AIRY
DRS	Data Reduction Software
FOV	Field Of View
FWHM	Full-Width at Half-Maximum
GS	Guide Star
GUI	Graphical User Interface
LBT	Large Binocular Telescope
LN	LINC-NIRVANA
LOST	Layer Oriented Simulation Tool
OSEM	Ordered Subsets Expectation Maximization
OTF	Optical Transfer Function
PSF	Point Spread Function
RLM	Richardson Lucy Method
RON	Read-Out Noise
SNR	Signal-to-Noise Ratio
SR	Strehl Ratio

5 References

- Anconelli B., Bertero M., Boccacci P., Lanteri H., and Correia S., 2004, *Deconvolution methods for LINC/NIRVANA data reduction*, in “New Frontiers in Stellar Interferometry”, ed. W. A. Traub, SPIE Proc. Vol. **5491**, 932-943.
- Anconelli B., Bertero M., Boccacci P., and Carbillet M., & Lanteri H., 2005a, *Restoration of interferometric images - III. Efficient RL-like methods for LINC/NIRVANA data reduction*, A&A **430**, 731-738.
- Anconelli B., Bertero M., Boccacci P., and Carbillet M., 2005b, *Restoration of interferometric images - IV. An algorithm for super-resolution of stellar systems*, A&A **431**, 747-756.
- Bertero M., and Boccacci P., 1998, *Introduction to Inverse Problems in Imaging*, IoP Publishing, Bristol.
- Bertero M., and Boccacci P., 2000a, *Application of the OS-EM method to the restoration of LBT images*, A&A Suppl. **144**, 181-186.
- Bertero M., and Boccacci P., 2000b, *Image restoration methods for the Large Binocular Telescope (LBT)*, A&A Suppl. **147**, 323-333.
- Bertero M., Boccacci P., Correia S., Richichi A., 2000c, *Tomographic methods for the restoration of LBT images*, in “Interferometry in Optical Astronomy”, eds. P.J. Lena, A. Quirrenbach, Proc. SPIE Vol. **4006**, 514-522.
- Carbillet M., Correia S., Boccacci P., and Bertero M., 2002a, *Restoration of interferometric images - II. The case-study of the Large Binocular Telescope*, A&A **387**, 744-757.
- Carbillet M., Correia S., Boccacci P., and Bertero M., 2002b, *Performance of the restoration of interferometric images from the Large Binocular Telescope - the effects of angular coverage and partial adaptive optics correction*, in “Interferometry for Optical Astronomy II”, ed. W. A. Traub, Proc. SPIE Vol. **4838**, 444-455.
- Correia S., Carbillet M., Richichi A., Bertero M., Boccacci P., 2000, *Large Binocular Telescope image restoration using simulated adaptively corrected point-spread functions*, in “Interferometry in Optical Astronomy”, eds. P.J. Lena, A. Quirrenbach, Proc. SPIE Vol. **4006**, 650-658.
- Correia S., Carbillet M., Fini L., Bertero M., Boccacci P., Vallenari A., Richichi A., and Barbati M., 2001, *AIRY: Astronomical Image Restoration in interferometry*, in “Astronomical Data Analysis Software and Systems **X**”, eds. F. R. Harnden Jr., F. A. Primini, and H. E. Payne, ASP Conf. Ser. Vol. **238**, 404-407.
- Correia S., Carbillet M., Boccacci P., Bertero M., and Fini L., 2002, *Restoration of interferometric images - I. The software package AIRY*, A&A **387**, 733-743.
- Hudson H. M., and Larkin R. S., 1994, *Accelerated image reconstruction using ordered subsets of projection data*, IEEE Trans. Med. Im. **13**, 601-608.
- Roddier C., Roddier F., Northcott, J., Graves J. E., and Jim K., 1996, *Adaptive optics imaging of GG Tauri: optical detection of the circumbinary ring*, ApJ **463**. 326-335.

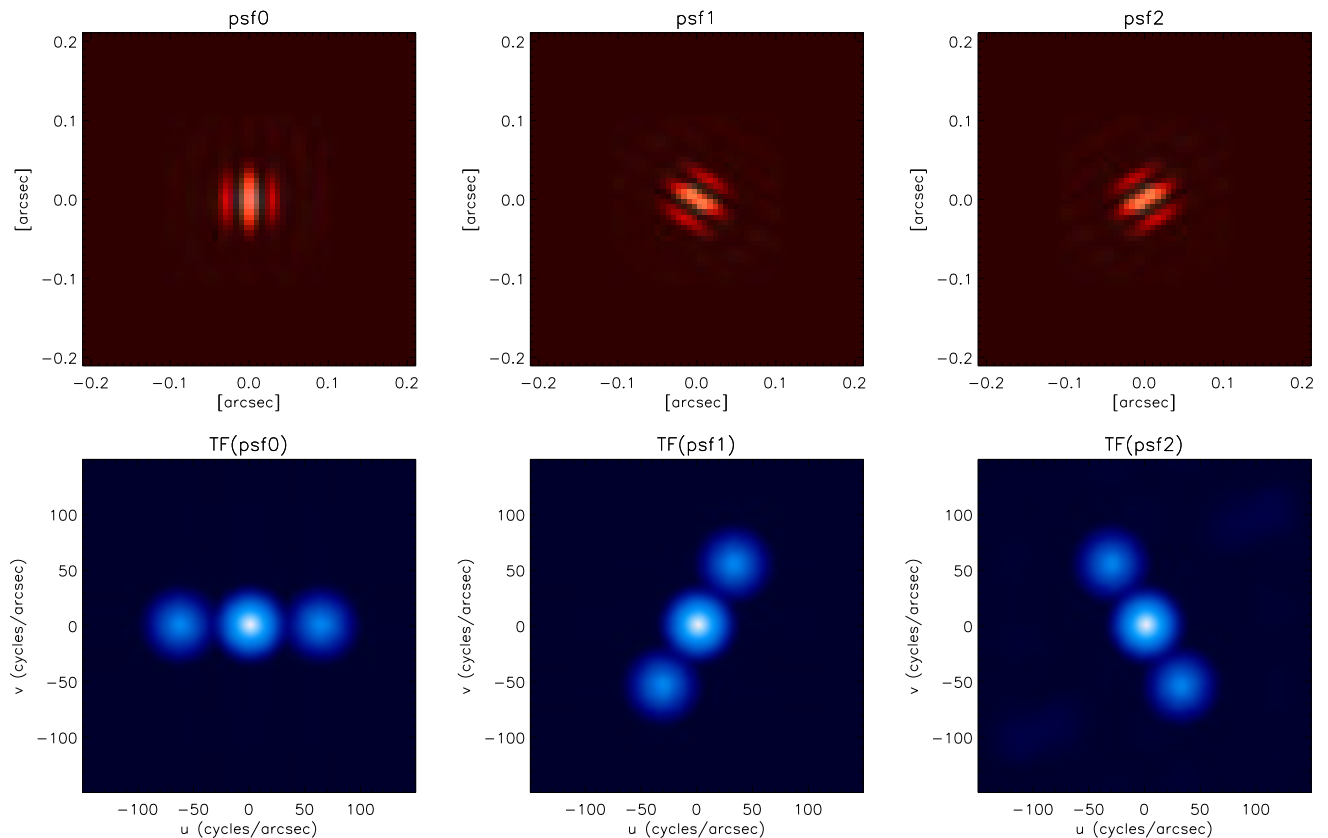


Figure 1: Top: LBT interferometric PSFs at (relative) position angles of 0° , 60° , and 120° . Bottom: the corresponding OTFs showing the u, v coverage.

- Snyder D. L., Hammoud A. M., and White R. L., 1993, *Image recovery from data acquired with a charge-coupled-device camera*, J. Opt. Soc. Am. **A10**, 1014-1023,
- Vio R., Nagy J., Tenorio L., and Wamsteker W., 2004, *A simple but efficient algorithm for multiple-image deblurring*, A&A **403**, 403-410.
- Wood K., Crosas M., and Ghez A., 1999, GG Tauri's circumbinary disk: models for near-infrared scattered-light images and ^{13}CO ($J = 1 \rightarrow 0$) line profiles, ApJ **516**, 335-341.

6 Introduction

LINC-NIRVANA is a unique instrument which will require efficient and accurate methods for multiple-image deconvolution. Here we outline our approach to the problem.

LN will provide different images of the same target corresponding to different orientations of the baseline, hence images with different coverage in the u, v plane. For each image, this coverage consists approximately of three discs: a central one, which is just the coverage of a 8.4 m telescope, and two side-lobes, which are shifted versions of the central one. Therefore, each image contains the information of an 8.4 m telescope with additional information, provided by interferometry, contained in the two side-lobes. This situation is illustrated in Fig. 1 where we show the PSFs corresponding

to three equi-spaced position angles and the corresponding OTFs.

The problem is to get a unique high-resolution image from the different images corresponding to different position angles. RLM can do this but it is slow: in the case of $p > 1$ images, the computational burden of each iteration is approximately increased by a factor p with respect to the single-image case. Therefore, we looked for accelerated versions of the multiple-image RLM. The most important of them is the OSEM algorithm proposed by Hudson & Larkin (1994) for emission tomography. When this approach is used, each iteration is a single-image iteration, the p images being processed cyclically. Moreover, further accelerated versions of OSEM have been investigated and implemented, so that we can roughly say that a gain of a factor 10 with respect to standard multiple-image RLM has been obtained.

According to our experience, and taking into account the features of astronomical images which can contain objects with different angular scales, very different magnitudes, and therefore also very different local SNR, we think that two different classes of deconvolution methods will be required for LN imaging:

- *General purpose methods*, computationally efficient as far as possible, to be used as a fast post-processing tool, in order to identify the main features of the observed object. The accelerated version of OSEM we have developed could be used for this task.
- *Dedicated methods*, developed for particular classes of objects with particular features. Due to the novelty of LN imaging, it may be useful to develop specific methods for at least a few important classes of astronomical objects.

All the methods we have investigated and implemented in the software package AIRY assume space invariance of the PSFs. This assumption is not satisfied in the real world of LN, even if our numerical simulations have demonstrated that an AO correction with low SR but good uniformity may be preferred as compared to an AO correction with high SR but low uniformity (see Section 12.2).

7 The model of image formation

In this document $N \times N$ arrays are denoted by bold letters. Let us assume that we have p images acquired with LN, corresponding to p different orientations of the baseline and denoted by $\mathbf{g}_1, \mathbf{g}_2, \dots, \mathbf{g}_p$. Then, if $\mathbf{g}_j(m, n)$, ($j = 1, \dots, p$) is the value of one of these images at pixel m, n , according to the model of image formation, proposed by Snyder et al. (1993) for images acquired with a CCD camera, we can write:

$$\mathbf{g}_j(m, n) = \mathbf{g}_{\text{obj},j}(m, n) + \mathbf{g}_{\text{back},j}(m, n) + \mathbf{r}_j(m, n) \quad , \quad (1)$$

where: $\mathbf{g}_{\text{obj},j}(m, n)$ is the number of photoelectrons due to object radiation; $\mathbf{g}_{\text{back},j}(m, n)$ is the number of photoelectrons due to external and internal background; $\mathbf{r}_j(m, n)$ is the read-out noise due to the amplifier. The first two terms are realizations of independent Poisson processes (photon noise), so that their sum is also a Poisson process and its expected value is given by:

$$E\{\mathbf{g}_{\text{obj},j}(m, n) + \mathbf{g}_{\text{back},j}(m, n)\} = (\mathbf{K}_j * \mathbf{f})(m, n) + \mathbf{b}_j(m, n), \quad (2)$$

where: \mathbf{K}_j is the point spread function (PSF), corresponding to the j -th orientation of the baseline (we assume, for simplicity, space-invariance); \mathbf{f} is the object array, formed by the average numbers of photons emitted at the pixels of the object domain and collected by the telescope; $\mathbf{b}_j(m, n)$ is the

expected value of the background. In the following, we will denote by A_j the matrix which is defined by the convolution product with the PSF \mathbf{K}_j :

$$A_j \mathbf{f} = \mathbf{K}_j * f, \quad (3)$$

and by A_j^T the transposed matrix.

In Eqs. 1 and 2, we assume that a pre-processing of the images has been performed, in order to correct for nonuniform quantum efficiency, bad pixels etc. Moreover, we will assume that the PSFs are normalized in such a way that the sum of their pixel values is one. In such a case, $\mathbf{K}_j(m - m', n - n')$ is the probability that a photon, emitted at pixel m', n' and collected by the telescope, is detected at pixel m, n .

Finally, the last term in Eq. 1 is the realization of an independent Gaussian process with expected value r and variance σ^2 (white noise). In the module ADN of AIRY (see [1]), which has been used for our numerical simulations, images are generated according to this model, even if only external background is considered while the expected value of the RON is set to zero. Moreover the background is supposed to be uniform over the field (after flat-fielding, of course), so that it is represented by constant arrays ($\mathbf{b}_j(m, n) = b_j$).

8 The image deconvolution method

For the convenience of the reader, we give here the extension of RLM to multiple-image deconvolution, as derived in Bertero & Boccacci (2000b):

$$\mathbf{f}^{(k+1)} = \frac{1}{p} \mathbf{f}^{(k)} \sum_{j=1}^p A_j^T \frac{\mathbf{g}_j}{A_j \mathbf{f}^{(k)} + \mathbf{b}_j}. \quad (4)$$

This method is implemented in the module DEC of AIRY and, even if it is slow, it may be used as a reference deconvolution for checking the accuracy of the accelerated methods, whose convergence is not proven theoretically. Moreover, module DEC of version 2.0 of AIRY contains the following accelerated version of OSEM:

- compute c , defined by:

$$c = \frac{1}{p} \sum_{j=1}^p \sum_{m,n=0}^{N-1} \{\mathbf{g}_j(m, n) - \mathbf{b}_j(m, n)\} ; \quad (5)$$

- choose an initial $\mathbf{f}^{(0)} \geq 0$ such that its total flux coincides with c (in general, a uniform image);
- given $\mathbf{f}^{(k)}$, set $j = (k + 1) \bmod p$ and compute:

$$\tilde{\mathbf{f}}^{(k+1)} = \mathbf{f}^{(k)} \left(A_j^T \frac{\mathbf{g}_j}{A_j \mathbf{f}^{(k)} + \mathbf{b}_j} \right)^\omega, \quad \tilde{c}^{(k+1)} = \sum_{m,n=0}^{N-1} \tilde{\mathbf{f}}^{(k+1)}(m, n); \quad (6)$$

- set:

$$\mathbf{f}^{(k+1)} = \frac{c}{\tilde{c}^{(k+1)}} \tilde{\mathbf{f}}^{(k+1)}. \quad (7)$$

This algorithm is derived in Anconelli et al. (2005a). The parameter ω is an *acceleration exponent*. If $\omega = 1$ we obtain the standard OSEM algorithm, in the form proposed in Bertero & Boccacci (2000a) for the case of zero background. In hundreds of numerical experiments, we have verified that this algorithm provides the same results of the algorithm of Eq. 4, with a gain in computation time of the order of $4/(3p+1)$. In the probably frequent case of 3 images, the computation time of OSEM is about 40 % of that of RLM, while, in the case of 4 images, is about 30 %. However, the important feature of this algorithm is that, for a given global SNR of the p images, *the computation time is independent of the number of images*, a property which can be very useful when one must replace a long exposure with several short ones in order to avoid smearing effects.

If $\omega > 1$, one can obtain a reduction in the number of iterations by a factor ω , hence an acceleration of the OSEM algorithm. However, the algorithm may not converge if ω is too large. The optimal choice of ω may depend on the object, SNR etc.

In a set of numerical experiments, intended to estimate the maximum value of the acceleration exponent compatible with the convergence of the algorithm, we have used eleven different nebulae observed with the Hubble Space Telescope and a binary star. These objects, shown in Fig. 2, are pushed far-away in order to match an angular resolution relevant for the 22.8 m equivalent aperture of LBT. For example, the young stellar object (YSO) IRAS 04302+2247, which is one of the diffuse objects and is also used for numerical simulations described in Section 9, is pushed to 1.4 Kpc instead of its actual distance of 140 pc. All these objects are 128×128 pixels and correspond to an extension of $\sim 0''.85$ (the pixel size is 6.67 mas, actually 5.11 in LN). The binary system consists of two stars with the same magnitude and an angular separation which can just be resolved by LBT in K-band. (~ 25 mas).

Images are generated by assuming ideal PSFs (corresponding to the three position angles of Fig. 1), an integration time of 20 min, a sky background value of $12.5 \text{ mag}''^{0.2}$ (K-band), a RON of $2 e^- \text{ rms}$, and a total transmission of 30%. Moreover, for each diffuse object, we use three different magnitudes, arbitrarily fixed to 14, 15 and 16. An increase in magnitude is equivalent to a decrease of the SNR in the observed images. Therefore, we consider 33 diffuse objects. The results of our experiments can be summarized as follows: for all the diffuse objects we have considered, we can use $\omega = 3$ if $m = 14$, $\omega = 5$ if $m = 15$ and $\omega = 8$ if $m = 16$. As a rule, the acceleration exponent increases for decreasing SNR, so that when the SNR is low, the algorithm can be very fast: the reduction in the number of iterations with respect to OSEM is just given by ω , without significant modification of the restoration error. This is the minimum value of the relative rms error defined by:

$$\rho_{\text{rel}}^{(k)} = \frac{\|\mathbf{f}^{(k)} - \mathbf{f}\|}{\|\mathbf{f}\|} , \quad (8)$$

where $\|\cdot\|$ is the Euclidean norm (square root of the sum of the squares of the pixel values), \mathbf{f} is the original object and $\mathbf{f}^{(k)}$ is the result of the k -th iteration. We have obtained an average restoration error of 9% for $m = 14$, 10% for $m = 15$ and 13% for $m = 16$, with corresponding average numbers of iterations of 350, 125 and 50. Without acceleration, the average numbers of iterations are, respectively, 1050, 625 and 400. However, it should be pointed out that the optimal number of iterations depends strongly on the specific object to be restored.

Similar results have been obtained in the case of the binary system: we can choose increasing values of the acceleration exponent for fainter magnitudes.

As a general rule, the algorithm with $\omega = 2$ is convergent for all objects and SNR considered in this and other numerical experiments, so that this acceleration exponent can be used safely. However, the simulation studies described in the following Sections were performed by taking $\omega = 1$, since the

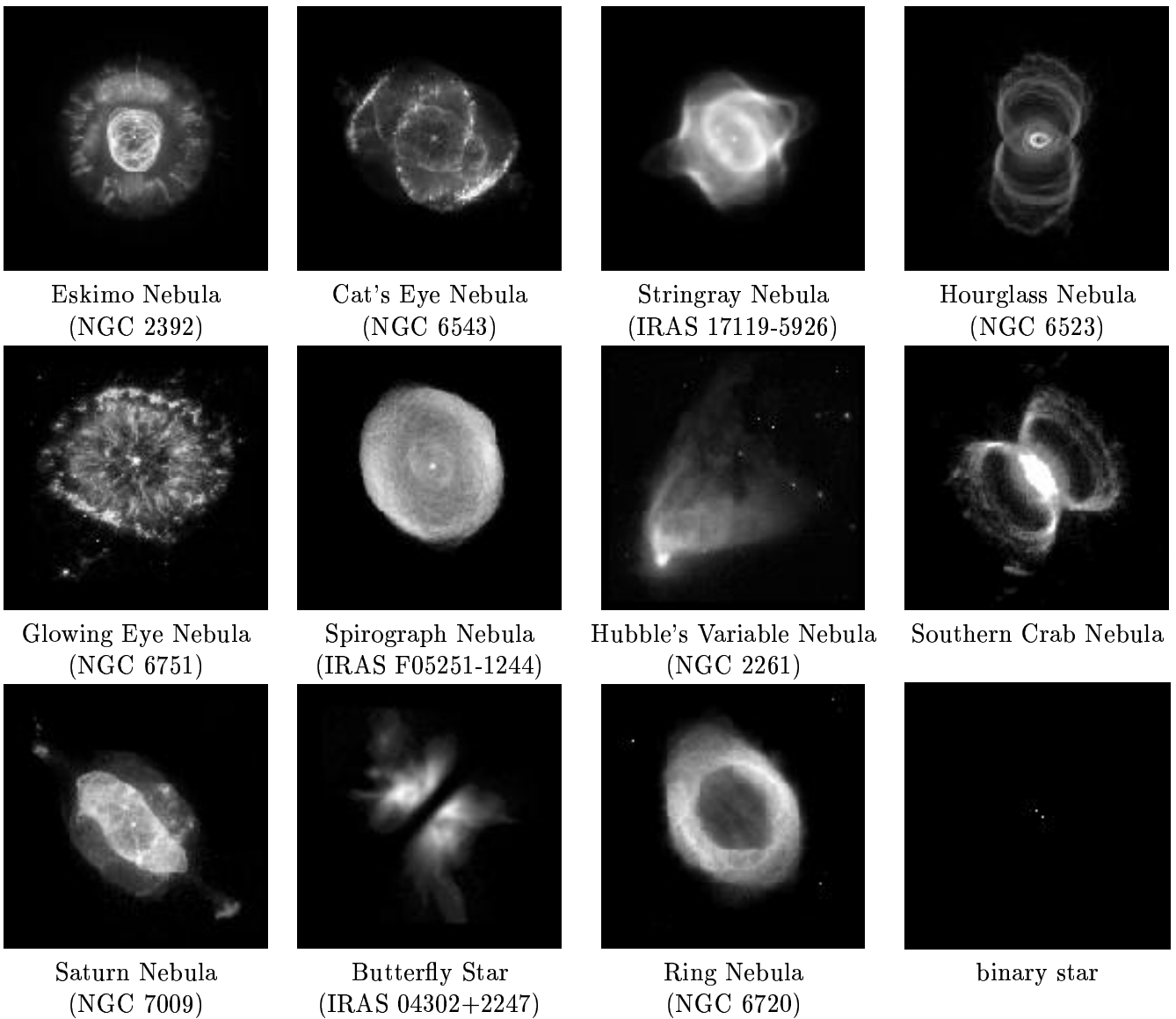


Figure 2: The objects used in the numerical experiments for the estimation of the acceleration exponent. Note that these are all complex objects (except the binary star) for which conventional co-axial interferometry is unsuitable.

possibility of taking $\omega = 2$ is a recent result.

9 Resolution of binary systems

A first relevant example is the case of binary stars with different angular separations and magnitude differences, since it allows us to investigate the fundamental limits of LN imaging. We restricted ourselves to the case of perfectly co-phased and AO-corrected PSFs, as well as to complete coverage of the u, v plane (see Correia et al., 2002). Therefore, we first describe the set of the PSFs used in our simulations, assuming that they correspond to the observation of an object with a suitable declination.

9.1 The interferometric PSFs and other parameters

We consider a set of LBT interferometric PSFs corresponding to the observation of an object with a declination of $+80^\circ$, assuming that observation is limited to airmass < 2 . More precisely we assume 6 observations equi-spaced in time in the allowed range of hour angles, that is between -5 h and $+5$ h. This corresponds to a range of position angle of $\sim 200^\circ$, thus providing complete coverage of the u, v plane (see Eq. 9 below).

We assume an integration time per baseline of about 20 min. During this integration time and for the declination we are considering, the average rotation of the baseline is of about 5° in position angle. This effect is taken into account in the computation of the PSFs by integrating over the position angles indicated above. The filter used is the K broad-band filter, and we correct for the spectral width of the filter ($\Delta\lambda=400$ nm) by integrating also over λ .

The spatial sampling adopted for all the interferometric PSFs used in this simulation is 3 pixels per FWHM of the fringes, where the FWHM is equal to λ/B , with B the total baseline length (22.65 m since the effective diameter of each mirror is 8.25 m, due to the adaptive secondary mirror of the LBT being the entrance pupil) and λ the filter central wavelength (here $2.2 \mu\text{m}$).

Other parameters used in our simulations are: total efficiency (mirror+optics+detector) of 25%, sky background brightness of $12.5 \text{ mag/arcsec}^2$ and a RON of $2 e^-$ rms. This can only be achieved by hybrid read-out techniques. Specification is $18 e^-$.

9.2 Intrinsic limits in the restoration of the parameters of binary stars

To investigate the intrinsic limitations in the reconstruction of binary stars with different angular separations ρ and magnitude differences Δm , we consider five different binary stars with increasing values of ρ and Δm . The observed images are simulated by means of the modules CNV and ADN of AIRY (see [1]).

- (1) the binary is poorly separated ($\rho=\lambda/B$, where B is the maximum baseline of LN), but has a reasonable magnitude difference ($\Delta m=1$).
- (2) the binary can be resolved by the maximum baseline ($\rho=2\lambda/B$), but not by each single pupil with diameter $D=8.25$ m (for LN $B/D \simeq 2.75$), and has a reasonable magnitude difference ($\Delta m=1$).

- (3) the binary has the same separation ($\rho=2\lambda/B$) as in (2), but a larger magnitude difference ($\Delta m = 5$).
- (4) the binary is well separated ($\rho=5\lambda/b$), but has a magnitude difference $\Delta m=9$.
- (5) the binary is even more separated ($\rho=15\lambda/B$), but has a magnitude difference $\Delta m=13$.

The first example can be considered as a limiting case for astrometry (see, however, Section 14), and the last three examples for photometry. We consider a case of high SNR, since we assume 20 min integration time per baseline and a main component magnitude $K=10$.

The results are shown in Fig. 3, where the errors in the retrieval of the three binary parameters (angular separation ρ , position angle PA and magnitude difference Δm) are plotted as functions of the number of iterations.

As expected, it is much more difficult to retrieve the parameters if the companion is closer to or much fainter than the main component. More precisely, in the first two cases (same magnitude difference but different angular separation), the accuracy is higher when the angular separation is larger even if in both cases results are quite good and the correct values are reached after a rather small number of iterations (very small in the second case).

In the second and third case (same angular separation but different magnitude difference), the increase in Δm implies that a higher number of iterations is required for extracting the weak companion from the remaining sparse energy of the main component. However, after detection, the retrieved binary parameters converge to rather accurate values. The effect increases for increasing magnitude difference. Indeed the detection of the companion takes place after ~ 50 iterations for the ($\rho=5\lambda/B$, $\Delta m=9$) binary and after ~ 200 iterations for the ($\rho=15\lambda/B$, $\Delta m=13$) binary; then the parameters converge to the correct values, with the exception of the angular separation of the ($\rho=15\lambda/B$, $\Delta m=13$) case.

In conclusion, for all binaries considered here except one (the last case), the parameters converge to the correct values, although with different convergence rates. As follows from Figure 3, the best accuracy in the evaluation of the angular separation is about 1 mas in the first four cases (ideal PSFs).

10 Reconstruction of diffuse objects

We consider here the case of an object with an extended and diffuse shape: an embedded young stellar object, also known as a Class I object, derived from HST near-infrared observations of IRAS 04302 +2247. This is a remarkable object showing a bipolar scattered light nebulae and a totally opaque dust lane, probably featuring a large optically thick circumstellar disk seen edge-on. We scale the image to have a $0.85 \times 0.85''$ extension, so that our object is more distant by a factor ~ 10 than the original one, i.e. about 1.4 kpc. With such a distance and the $K=15$ magnitude that we set here, instead of the true $K=10.9$, our simulated object is intrinsically brighter by roughly 1 mag. With this brightness and the integration time considered in all our simulations (20 min), the single baseline image peak SNR is ~ 180 . Figure 4 shows the object, as well as one of the observed images and the result of the reconstruction.

The accuracy of the reconstruction provided by the k -th iteration can be measured by computing the relative *rms* error defined in Eq. 8. If we plot $\rho^{(k)}$ as a function of the number of iterations k , we find a minimum at $k=263$, with a minimum value of 5.6% (the restored image of Fig. 4 corresponds

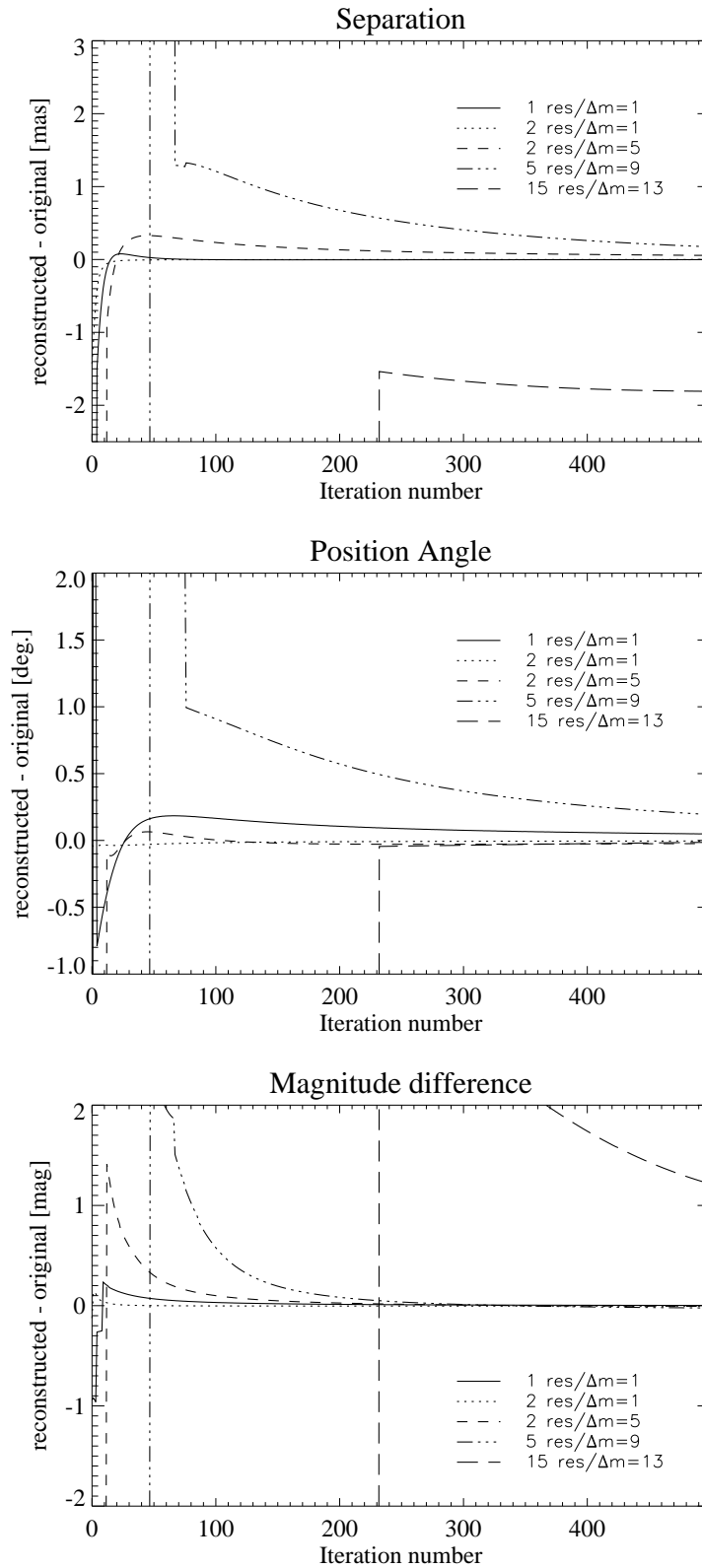


Figure 3: Restoration of binary parameters in the case of ideal PSFs and complete coverage of the u - v plane: error plots of the angular separation ρ , position angle PA and magnitude difference Δm , versus the number of iterations of the OSEM method, for the five cases defined in the text. In the legends “res” means λ/B .

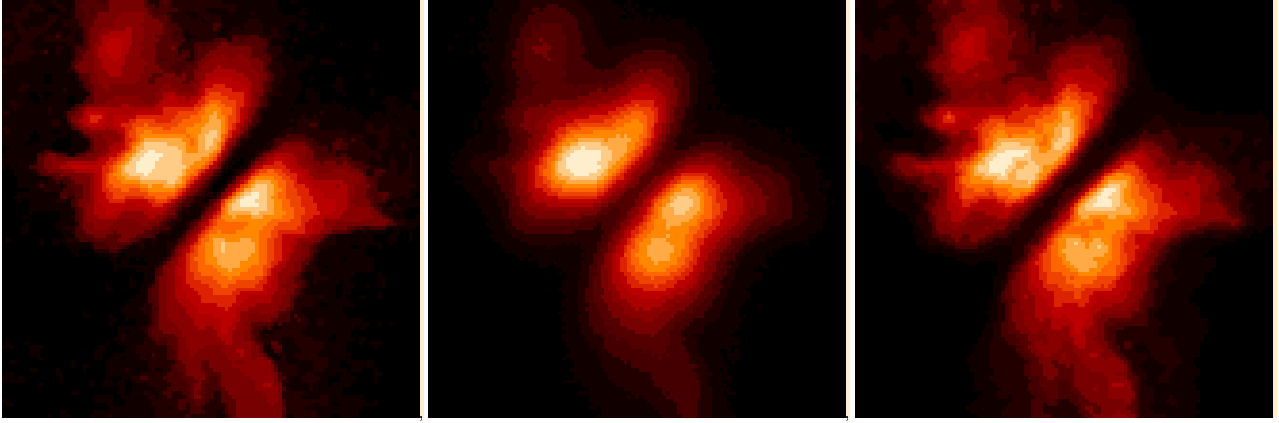


Figure 4: From left to right: the original object; the image corresponding to a position angle of $\sim 60^\circ$; the reconstructed image. The image extension is about $0.7''$. The gray scale is square root.

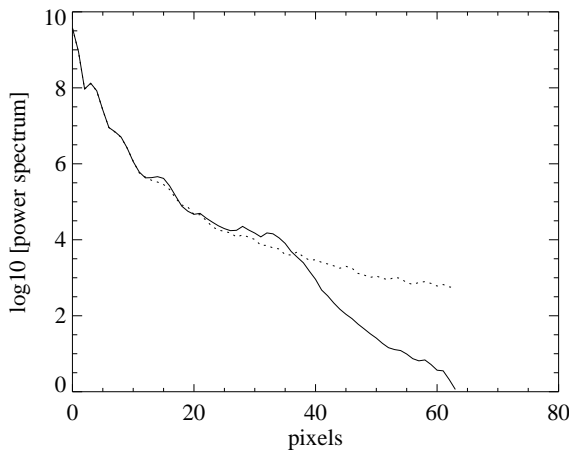


Figure 5: Profiles of the azimuthally averaged power spectra corresponding to the object and restored image shown in Fig. 5. Solid line corresponds to the restored image ($k = 263$), dotted-line to the object. The telescope cut-off frequency is located at $128/3 \simeq 40$ pixels.

to this minimum). We observe however that in this example the minimum is very flat so that after 70 iterations we already have a restoration error of about 7%. Such a restoration is not visually distinguishable from that given in Fig. 4.

We also checked the accuracy of the reconstruction of the power spectrum of the object. This is shown in Fig. 5, where we compare the profiles of the azimuthally averaged power spectra of the object and of the reconstructed image. As expected the two curves match fairly well up to the telescope cut-off frequency located at about 40 pixels.

11 Analysis of a simulated star cluster

The goal is to simulate high-resolution interferometric observations of a complex scientific object and to retrieve its scientific parameters after the image restoration process (Correia et al., 2001).

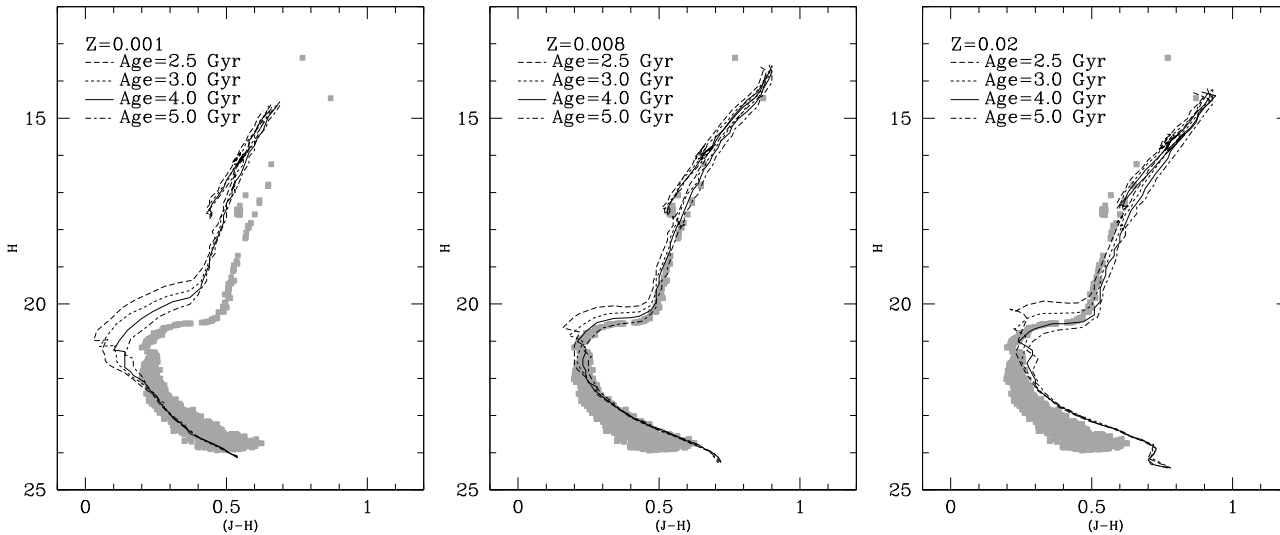


Figure 6: CMD of the star cluster in the plane H vs $(J-H)$. Detected stars are marked with squares and isochrones corresponding to different ages and metallicities (left: $Z=0.001$; center: $Z=0.008$; right: $Z=0.02$) are superimposed.

We have considered a star cluster composed of 1898 stars with the following characteristics: age 4.0 Gyr, metallicity $Z=0.008$, distance modulus=19 ($\simeq 63$ kpc), reddening=0, extension field= $10.24'' \times 10.24''$. Three object maps (2048×2048 pixels) were modeled in J, H and K bands. The resulting magnitude ranges were respectively 14.01-24.22, 13.25-23.63 and 12.89-23.56. Next we have simulated observations at 3 position angles (0° , 60° and 120°) for each band, and with 2000 s integration time for each position angle. Ideal PSFs have been assumed. Deconvolution was carried out for each band using 100 OSEM iterations. Detection and photometry on the restored frames were performed using Daophot, with a 25-sigma detection threshold and a 3 pixels (15 mas) aperture photometry diameter.

The CMD of the star cluster in the plane H vs $(J-H)$ is shown in Fig. 6. Detected stars are marked with squares and isochrones corresponding to different ages and metallicity values are superimposed. From a first visual inspection, we can derive the cluster's age and metallicity to be 4.0-5.0 Gyr and $Z \simeq 0.00$ respectively, a result which is in good agreement with the input parameters.

12 Partial angular coverage and angular smearing

In this Section we summarize results, reported in Carbillet et al. (2002a) and (2002b), about the effects of partial angular coverage and angular smearing on the quality of the reconstructed images. These effects are related to the object declination.

The position angle q depends on the object declination δ and the hour angle H as follows:

$$q = \arctan \left(\frac{\tan \phi \cos \delta - \sin \delta \cos H}{\sin H} \right), \quad (9)$$

Table 1: The range of the hour angle H and the corresponding range of the position angle q , field rotation velocity \dot{q} , and integration time Δt corresponding to an angular smearing of 5° , for different values of the object declination δ , in the case of LBT.

case	δ ($^\circ$)	range H ($^\circ$)	range q ($^\circ$)	\dot{q}_{max} (""/s)	\dot{q}_{min} (""/s)	Δt_{max} (min)	Δt_{min} (min)
wide	+80	204	216	17.3	14.2	20	16.0
narrow	-20	60	58	15.8	12.3	24	19.0
zenith	+30	142	135	271.0	4.5	72	1.1

where ϕ is the latitude of the observatory ($+32.667^\circ$ in the case of LBT). The implication is twofold. First: The range of position angles accessible during the night for an object at a given declination can be limited (i.e. less than 180°), implying an incomplete coverage of the u, v plane. Second: Due to the variation of the fringe pattern rotation rate during the night, the variation of position angle during the integration time can induce significant differences in angular range for different baseline orientations, especially when the object passes close to the zenith. We report in Table 1 the ranges corresponding to the three relevant cases we have selected: a "wide" case ($\delta = +80^\circ$), a "narrow" case ($\delta = -20^\circ$), and a (close to) "zenith" case ($\delta = +30^\circ$) (note that the reported ranges of position angle q are obtained by considering an airmass < 2). While the "wide" case provides a complete coverage of the u, v plane without problems of angular smearing, the "narrow" case leads to an incomplete angular coverage ($\sim 60^\circ$), and the "zenith" case corresponds to a significant variation of the position angle around $H = 0^\circ$ (up to ~ 270 "/s). In the last case the problem which naturally arises is the effect of the angular smearing, and hence its comparison with the effect of noise increasing if shortest exposures are considered in order to overcome the angular smearing effect.

We use as an astronomical test object a model of a young binary star consisting of a core binary star surrounded by a dusty circumbinary ring. The model is directly inspired by near-infrared observations of the T-Tauri binary star of the quadruple system *GG Tau*, and the subsequent interpretation and modeling (Roddier et al., 1996; Wood et al., 1999). This type of object is challenging for the restoration methods: it combines point-like features (the core binary star) and a diffuse one (the circumbinary ring), with high dynamic range between them, as can be seen in Fig. 7 [top]. We choose for the binary a separation of ~ 40 mas (twice the angular resolution of LBT in K-band but still unresolved by a single eye of the LBT) and a magnitude difference of 1. The circumbinary ring is characterized by an integrated K-magnitude of 15.25, with respect to 10 for the main component of the binary star. From the restored image, we then compute the error on the parameters of the core binary star (angular separation, position angle, and magnitude difference Δm). We also evaluate the restoration error of the morphological parameters of the circumbinary ring (radial intensity profile and azimuthal intensity profile), before and after applying a perfect PSF- subtraction of the core binary (hence extrapolating our results to the generic case of extended faint objects). Additional global parameters of our simulations are: total efficiency (mirror+optics+detector) of 25%, sky background of $12.5 \text{ mag}/''^2$ and RON of $2 e^-$ rms.

Figure 7 shows the difference between the "wide" and "narrow" angular coverage together with the result of the reconstruction of the complete testing object and of the circumbinary ring alone. Exposures of 20 min were considered (six for the "wide" case and three for the "narrow" case, distributed within the available angular range). As can be seen, the limitation in angular coverage still allows acceptable results.

Figure 8 [top] shows the effect of the angular smearing in the "zenith" case, which is evident in the

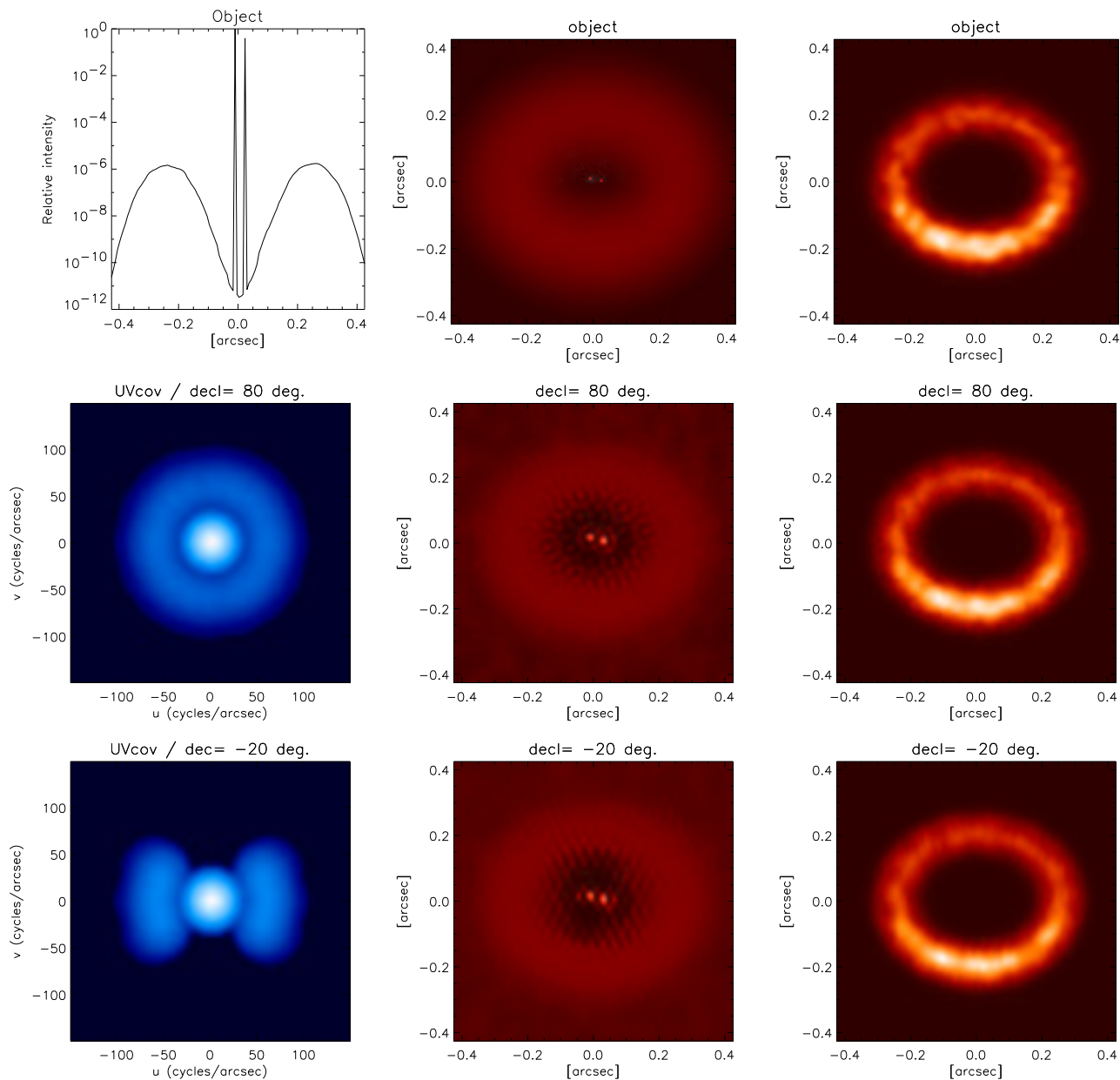


Figure 7: *Top, from left to right:* the log-cut of the *GG Tau*-like object in the direction of the binary axis; the whole object; the circumbinary ring alone. *Middle, from left to right:* the u, v coverage of the "wide" case; the corresponding restoration of the whole object; the corresponding restoration of the ring alone. *Bottom, from left to right:* the u, v coverage of the "narrow" case; the corresponding restoration of the whole object; the corresponding restoration of the ring alone.

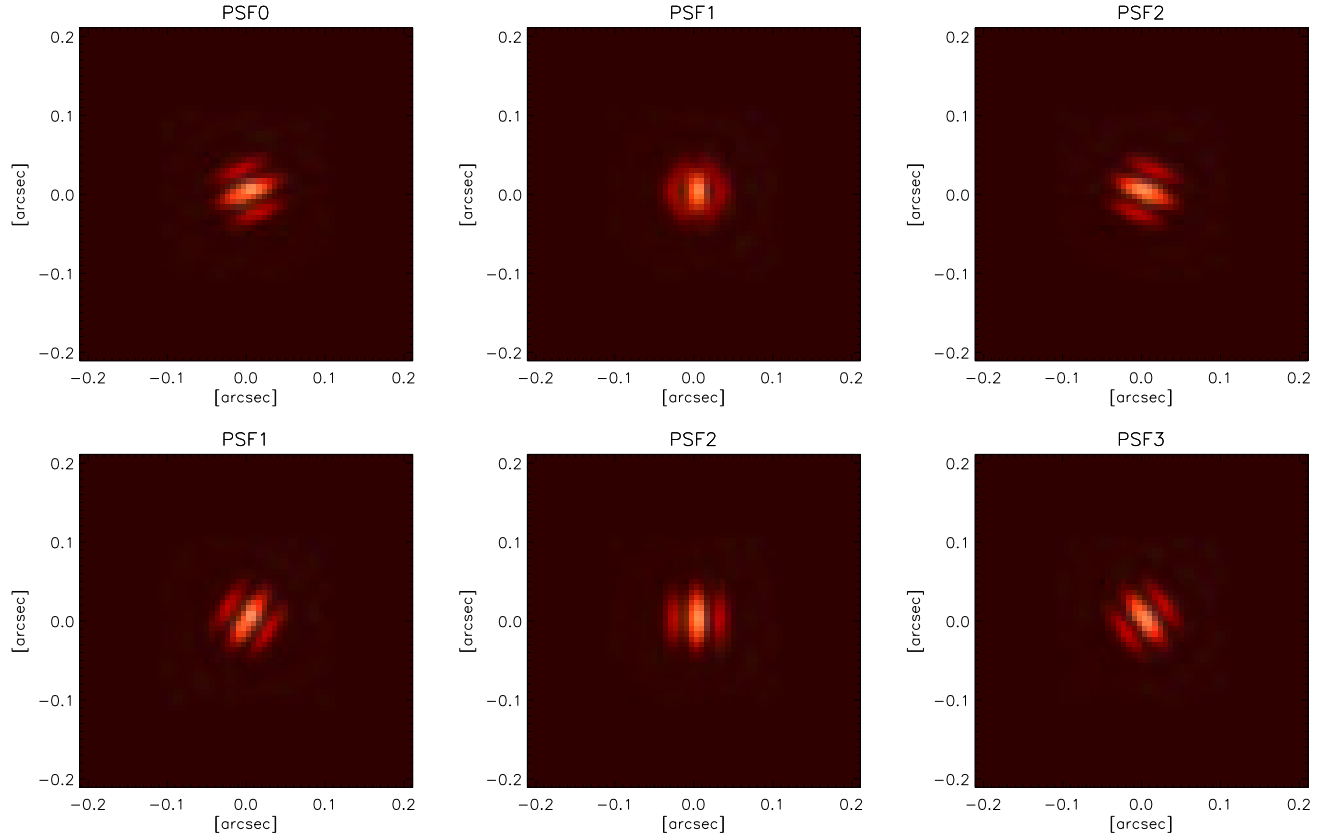


Figure 8: Top: the set of PSFs of the "zenith" case, showing the angular-smeard PSF (middle). Bottom: the three PSFs taken instead of the previous smeard one for the "zenith/5 baselines" case.

central PSF since this is obtained by integrating over 76° . In order to study this effect versus the lack of photons resulting from splitting the smeard images into three angularly equi-spaced short exposures of 1 min, we have considered the three additional PSFs represented also in Fig. 8 [bottom]. We call this last case the "zenith/5 baselines" case.

The comparison of the results obtained for the "wide", "narrow", "zenith" and "zenith/5 baselines" case is illustrated in Fig. 9, by plotting the reconstruction errors both of the azimuthal profile of the ring and of the magnitude difference of the core binary. Our main conclusions are the following:

- The accuracy in the retrieval of the core binary parameters is definitely better when the coverage is complete ("wide" case), or almost complete without angular smearing ("zenith/5 baselines" case), even if the absolute errors are remarkably small in all cases.
- While the use of short exposure images in order to overcome the problem of angular smearing (from the "zenith" case to the "zenith/5 baselines" case) provides a better precision in the restoration of the core binary parameters, practically at the same level of the "wide" case, this is not true for the circumbinary ring restoration where the expected effect of noise increasing is evident. Hence a trade-off between smearing and noise increasing has to be found when imaging extended faint objects.

A general remark is that only the high spatial frequencies (i.e. beyond the frequency corresponding to the cut-off frequency of the single pupil) are sensitive to the incomplete u, v coverage. The natural

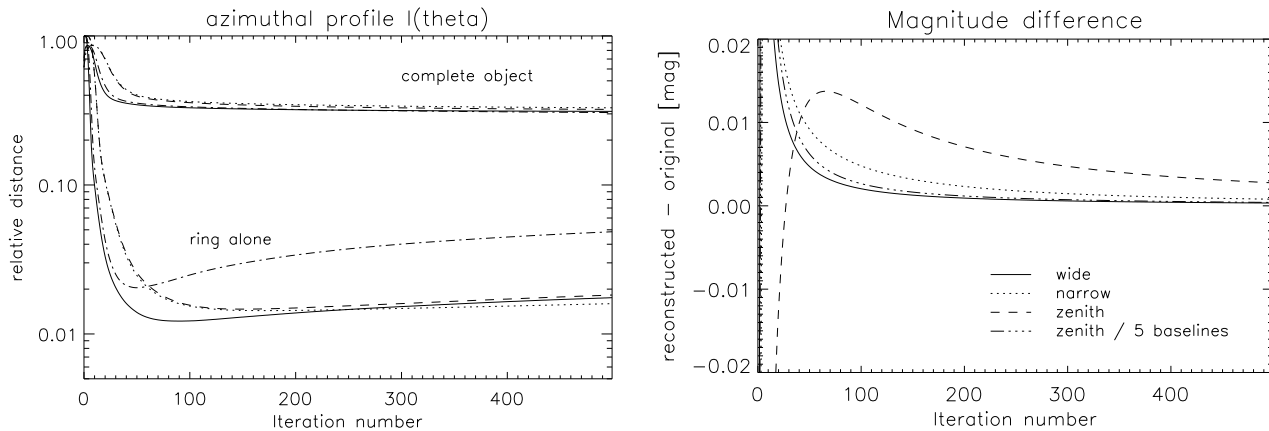


Figure 9: Plots of the restoration errors as functions of the number of iterations: in the case of the azimuthal profile of the circumbinary ring [left], and in the case of the difference of magnitude of the core binary [right].

attenuation of the two interferometric regions of the u, v plane by the OTF makes this limitation more critical for the case of objects with small and faint structures.

In addition, it is interesting to note that the ring curves show a global minimum around 100-200 iterations, whereas the binary curves tend to converge indefinitely. This feature of "semiconvergence" (see, for instance, Bertero & Boccacci, 1998) is well-known in the theory of iterative restoration methods and is clearly due to the phenomenon of "noise amplification". We can then conclude that the definition of a reliable stopping-rule would be of great help when dealing with real data.

12.1 Discussion

The simulations described above seem to indicate that the angular coverage and the smearing effect do not affect significantly the large-scale/ overall structure of the image nor the parameters of the binary, but only the convergence rate of the iterative method. If we also take into account the problem of noise amplification when dealing with faint extended objects or when using short exposures in order to suppress the smearing effect, we conclude that the possibility of implementing criteria for stopping the iterations should be considered.

13 Partial (and space-variant) Adaptive Optics correction

The effect of partial AO correction on a single-pupil telescope has the global consequence that the image of a point-source is not exactly an Airy disk, but a central core surrounded by a halo where the first Airy ring is typically broken. In the case of interferometry we also have to consider the differential piston that produces a motion of the fringe pattern along the baseline axis. In a similar way, the differential tip-tilt, resulting from the tip-tilt residuals of each single pupil that causes a global motion of the single images, has the effect of a bad superimposition of the two single-pupil envelopes, deforming the interferometric PSF. On the other hand, high-order residuals cause the interferometric PSF to be composed of a central fringed core together with a "speckle-ized" halo where each speckle-like feature is also fringed.

We are here interested in both the global level of AO-correction and space variance of the AO-corrected PSFs. Therefore, we consider two case-studies:

1. Starting from the known performance of the first-light AO system of LBT, and assuming that at least the single-conjugate phase of LINC-NIRVANA will show similar behaviour, we define different sets of parameters of our simulation of AO-corrected interferometric PSF leading to different global levels of AO-correction (coming from different magnitudes of the GS and subsequent parameters of the system). We therefore assume an object in K-band (sensing wavelength is $\sim R$) at a certain constant angular distance from the GS (here $15''$). The resulting sets of interferometric reference images (PSFs since the reference is supposed to be point-like) and object images are then assembled from observations at different position angles (here again 0° , 60° , and 120°), corresponding to three different exposures, and then to three different realizations of the turbulent atmosphere. The AO system behaviour is simulated with the software package CAOS. The differential piston is simply attenuated by a certain factor (no real simulation of its correction).
2. Assuming observation at a given global level of AO correction, we consider a given object at an increasing angular distance from the reference star. This is equivalent to considering an increasing anisoplanatism error that affects the AO correction. We then look at the difference between the reference PSFs and the object PSFs (and the effect on the reconstruction process), rather than at the global level of AO correction. The different sets of PSFs result this time from taking different angles between the two, i.e. different off-axis angles from the GS, ranging from 0° towards what we can call the "maximum angle of correction" θ_{\max} , which corresponds roughly to half the on-axis SR. Resulting median SRs of each set are: 94% (on-axis), 93%, 88%, 81%, and 53% (nearly θ_{\max}).

Figure 10 shows the result of one of the simulation runs looking at the global level of AO-correction. The instantaneous wavefronts during AO-correction are represented, together with the resulting on-axis reference PSF and binary star image at $15''$ off-axis.

13.1 Space-variance of the AO-corrected PSF

For this study we generate four sets of LN interferometric images by convolving the *GG Tau*-like object used in the previous Section, with the four sets of PSFs corresponding to the four SR median values indicated in point 2 (see above), and by perturbing the result with the sky background emission and the different kinds of noise. The obtained sets of images are then deconvolved by means of the corresponding reference PSFs. The results are evaluated again both in terms of the retrieval of the core binary parameters, and of the circumbinary ring profiles. In Figure 11 we plot, as functions of the number of iterations, the relative error on the difference of magnitude of the core binary star (right), and on the radial profile of the circumbinary ring (left).

As expected, when the reference star is closer to the object, hence the PSF estimation is better, the reconstruction of the object is also better. In any case, it should be noted that in the worst case scenario (SRs=94% & 53%), the error is less than 0.07 mag for the core binary Δm –which is small indeed, and $\sim 20\%$ for the radial profile of the circumbinary ring; with a quick convergence, since only ~ 100 iterations are required in all cases.

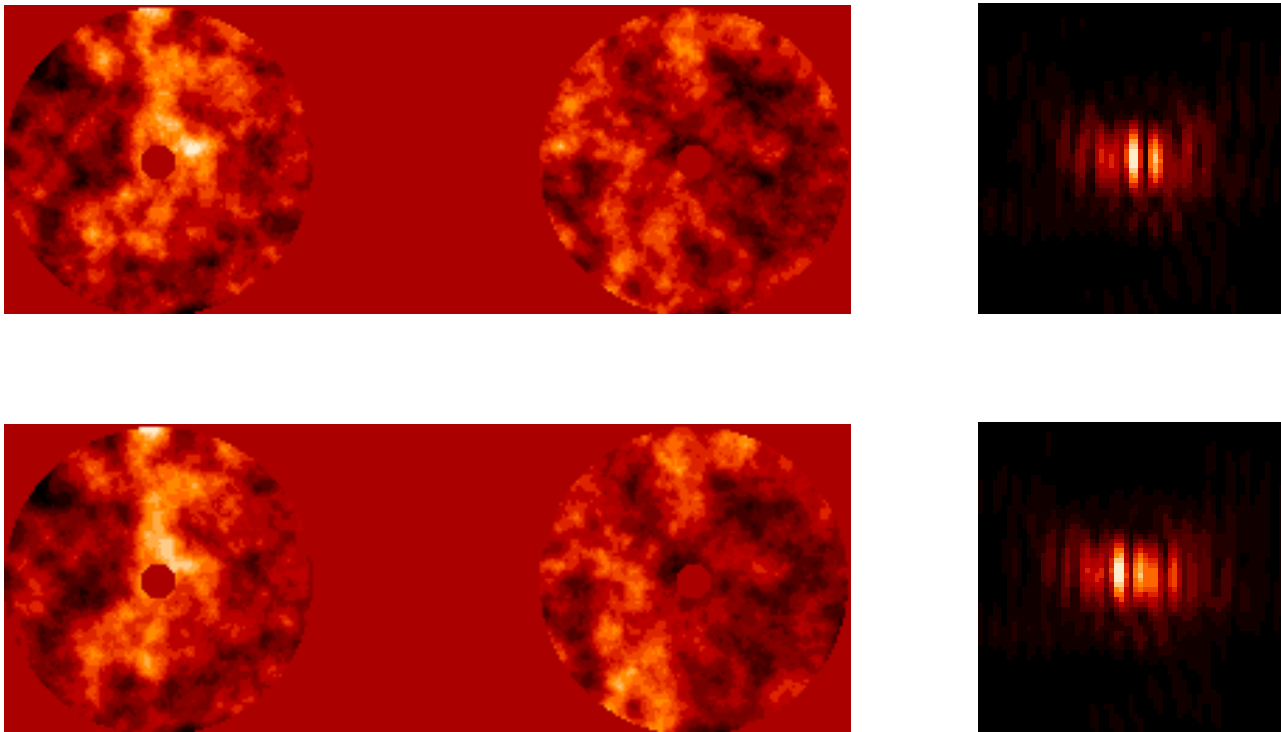


Figure 10: From left to right: wavefront residuals during AO-correction, and corresponding interferometric image: for the on-axis reference star [top], and for the binary star taken in Sec. 13.2 at 15'' off-axis [bottom]. This example corresponds to the GS @ $m_R=15.6$ of Table 2.

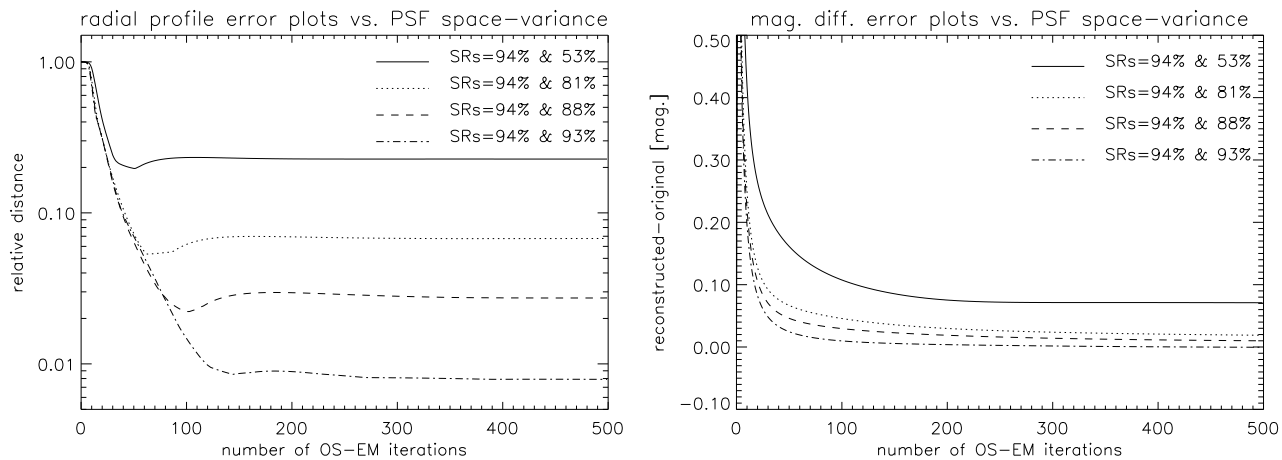


Figure 11: Plots of the relative error on the radial profile of the circumbinary ring [left] and on the difference of magnitude of the core binary [right], as functions of the number of iterations, for different levels of the space-variance of the AO-corrected PSF.

Table 2: R-magnitude of the GS used during AO correction, number of corrected mirror modes, range of additional differential piston residual considered, and resulting K-band SRs.

AO GS R-mag	mirror modes corrected	diff. piston rms [nm]	S_K @ 0° (reference/object)	S_K @ 60° (reference/object)	S_K @ 120° (reference/object)
9.6	496	~ 0	94.7 / 77.1	94.2 / 78.2	94.8 / 73.3
12.6	136	10–20	80.9 / 69.1	78.9 / 66.0	77.6 / 60.2
14.6	66	20–40	56.4 / 48.2	55.3 / 46.8	52.2 / 40.0
15.6	55	50–100	35.8 / 27.2	34.8 / 25.4	35.6 / 25.6
16.6	45	100–200	10.5 / 08.4	18.5 / 14.8	13.6 / 10.6

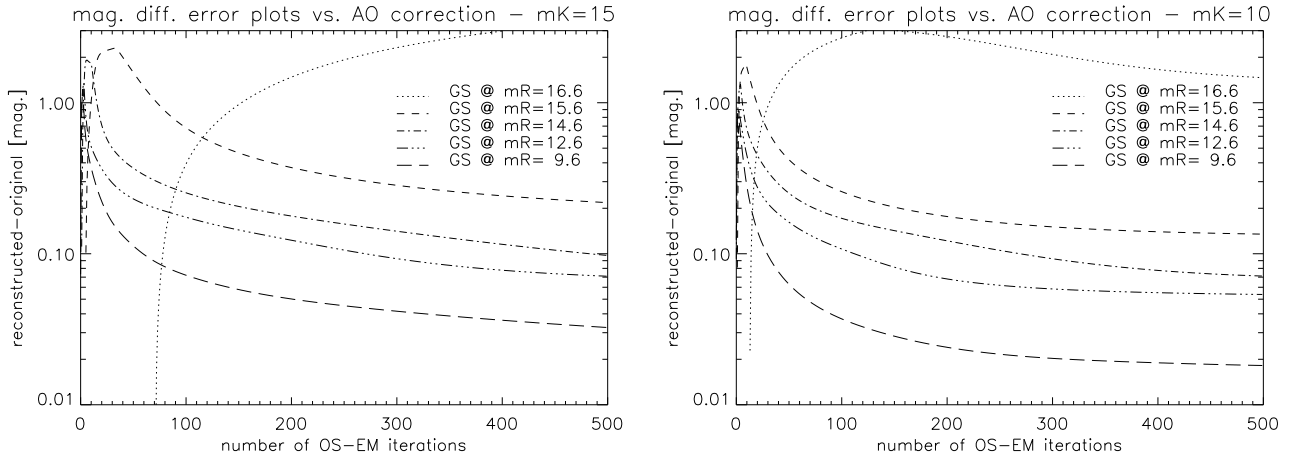


Figure 12: The error on the magnitude difference of the binary star, as a function of the number of iterations; the different plots correspond to different global levels of AO correction of the sets of interferometric images: [left] the case with a main component of K-magnitude 15; [right] the case with a main component of K-magnitude 10.

13.2 Global AO-correction quality

Table 2 is a résumé of the parameters and SRs obtained for the simulated situations of global level of AO-correction. The AO GS R-magnitude is reported, together with the number of corrected LBT 672 adaptive secondary mirror modes, the additional differential piston rms (no simulation of its adaptive correction), and the resulting SR in K-band for each set and each position angle.

In this way, five sets of reference PSFs are considered together with five sets of images of an astronomical object of interest. Moreover, we consider two objects: a binary star with a primary with $K = 15^{rmm}$, magnitude difference of 1, and angular separation ~ 45 mas; the *Butterfly Star*-like object already considered in Section 4, with an integrated K-magnitude of 14.

The results on the restoration of the binary star are reported in Fig. 12 [left]. While the error on the restoration of the difference of magnitude goes from ~ 0.03 mag to ~ 0.2 mag when going from the best case (GS @ $m_R=9.6$) to the case “GS @ $m_R=15.6$ ”, the worst-case scenario (GS @ $m_R=16.6$) is clearly not converging toward a reasonable solution: the PSF estimation is too bad in the last case ($\langle SR \rangle \sim 13\%$). The right-part of Fig. 12 shows the result of the same simulation but with a main component of K-magnitude 10: this is directly comparable with the previous results on the *GG Tau*-

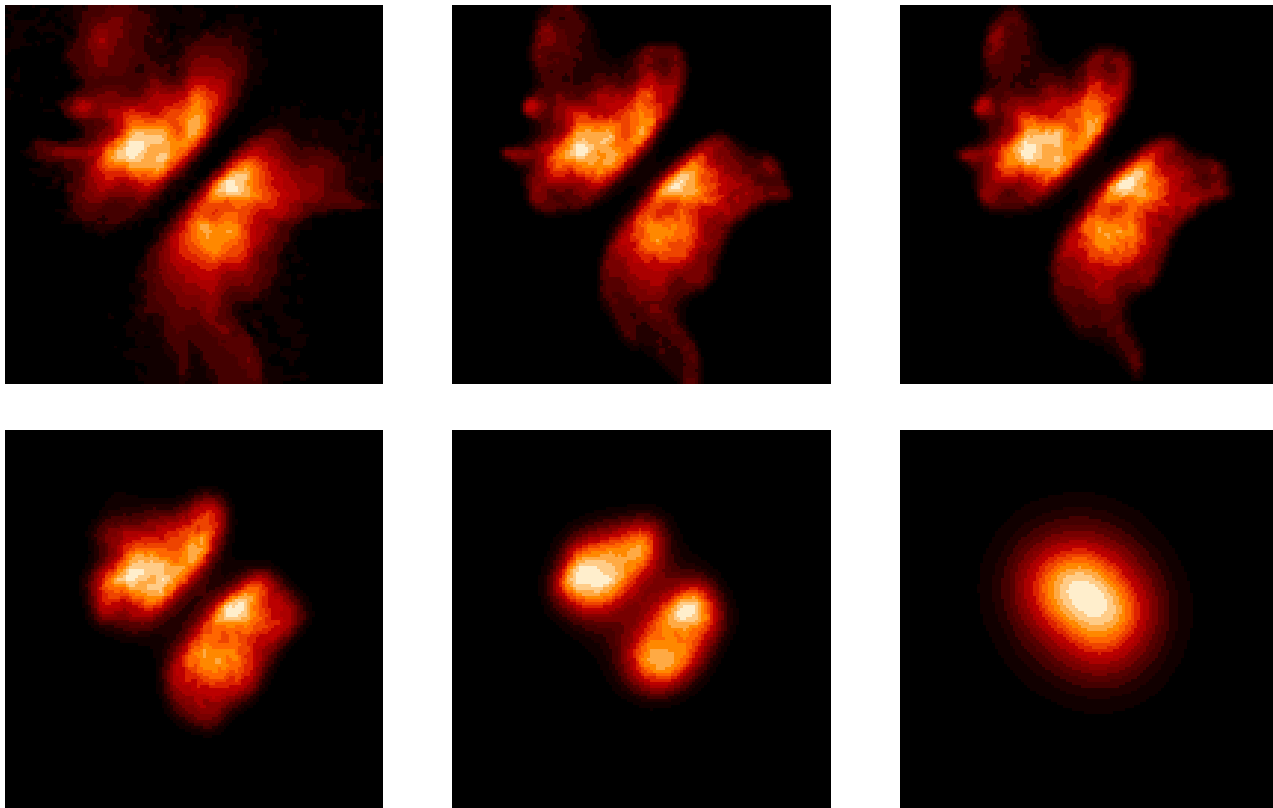


Figure 13: Reconstruction of the *Butterfly Star*-like object for different global AO quality. From left to right and from top to bottom: the object, the results of the reconstruction with decreasing global AO-correction quality as indicated in Table 2.

like object. We note that the result for GS @ $m_R=9.6$, which is very similar to the case "SRs=94% & 81%" of the previous Subsection, leads to exactly the same precision on the difference of magnitude (~ 0.02 mag). The results show once again that a major difference in the PSFs, this time mainly due to an increasing number of modes from the atmosphere that remain uncorrected (rather than to an increasing pure anisoplanatism error), and then a poorer estimate of the PSF corresponding to the images of the observed object, leads to a decreasing precision of the reconstruction, and even to a wrong one (see the worst case: "GS @ $m_R=16.6$ ").

Figure 13 shows the reconstructions obtained with the same sets of AO-corrected PSFs for the *Butterfly Star*-like object. The effect of the decrease of the global AO-correction quality is again evident: while the best case leads to a very good reconstruction, the high-frequency features are more and more badly reconstructed, with the bipolar feature not recognizable in the worst case. The degradation of the quality of the restoration with decreasing SR values can be understood in terms of SNR in the Fourier space.

13.3 Discussion

Concerning PSF uniformity, Fig. 14 shows the comparison between the restoration of the core binary star of our *GG Tau*-like object for the case of non-uniform PSFs ("SRs=94% & 53%" case), and for perfectly uniform PSFs at two different regimes of AO-correction: the "SRs=53% & 53%" case, and the SRs=94% & 94%" case. It is clear from these plots that uniformity is a main issue for this

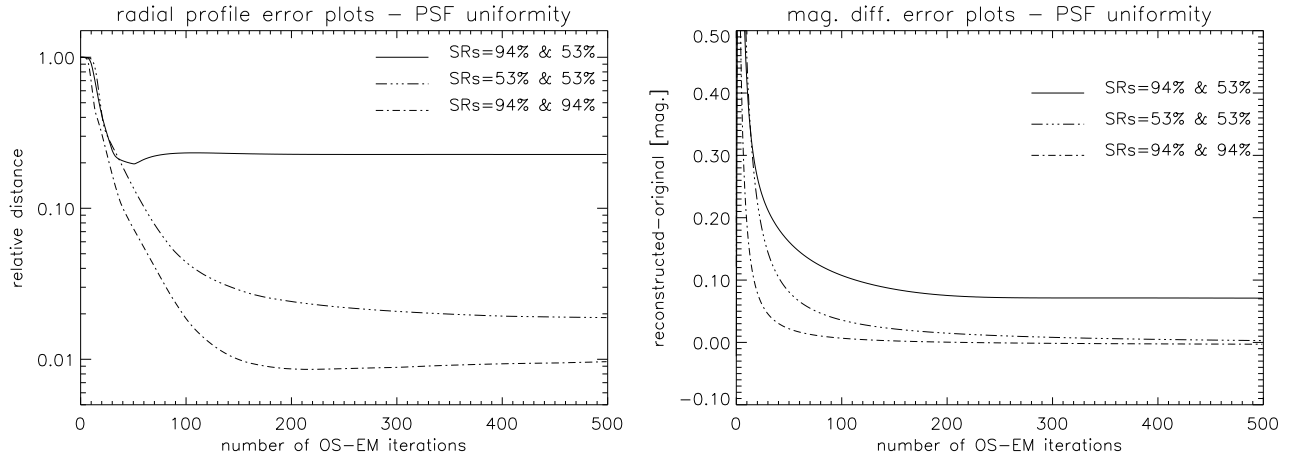


Figure 14: Relative error on the radial profile of the circumbinary ring [left] and on the difference of magnitude of the core binary [right], as a function of the number of iterations, in the case of a uniform-PSF MCAO system.

observational technique, even at the cost of a lower average SR, at least for the field of application we have considered. Such a condition, which may be satisfied by the MCAO system of LINC-NIRVANA, is also required by the model of image formation assumed in the deconvolution method and implies that the PSF obtained from a reference star provides a good approximation of the PSF which must be used in the process of image restoration. From the point-of-view of system design and strategy of AO-correction/observation, this is also interesting information.

14 An example of a two-step method: resolution enhancement

Thanks to the over-sampling provided by LINC-NIRVANA in K-band (about 4 sampling points within the diffraction limit), it is possible to design methods for improving the resolution in the imaging of unresolved stellar objects such as binary stars. The method we have proposed and validated is implemented in the module DEC of AIRY (see [1]) and consists of two steps, with the addition of a third one for improving the photometry. A detailed description is given in Anconelli et al. (2005b).

Step 1 - Apply the OSEM method to the detected images, using a constant array as initial guess and a number of iterations such that the restored object is sufficiently well localized. If the angular separation is not much smaller than the diffraction limit and the magnitude difference is small, it may happen, in the case of a binary, that the two stars are already resolved in this first step. In such a case, one can estimate their positions by computing the centroids and go directly to Step 3 for a more accurate estimate of their magnitudes.

If the two stars are not resolved, then go to Step 2.

Step 2 - Define the domain \mathcal{D} of the object by identifying the pixels where the flux of the result of Step 1 is greater than a selected threshold (for instance some percent of its maximum value); alternatively, one can take a disc with diameter equal to the diffraction limit and containing most of the flux of the reconstructed object.

Again apply the OSEM method to the detected images, but now initialized with the mask of the

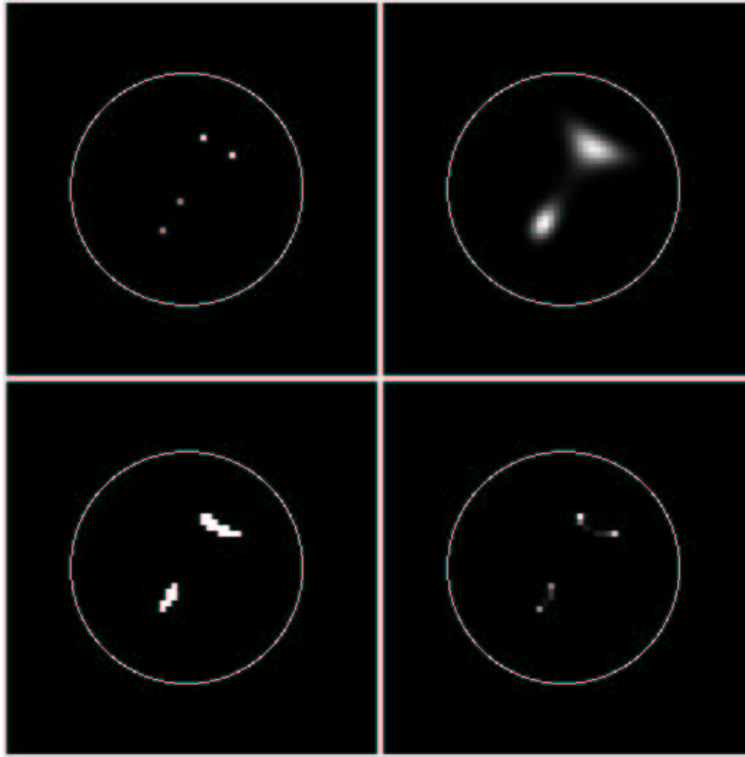


Figure 15: Upper-left panel: the object; upper-right: the reconstruction after 1000 OSEM iterations (first step); lower-left: the mask obtained with a thresholding of the previous reconstruction (50 % of the maximum value); lower-right: the restoration after 1000 OSEM iterations, initialized with the previous mask (second step). The radius of the circle shown in each picture is λ/B .

domain, namely a function which is constant over the domain and zero elsewhere. Thanks to the multiplicative structure of OSEM, each iterate is also zero outside the selected domain; if, after a number of iterations, the two stars are separated, their positions are obtained by computing their centroids.

Figure 15 shows an example of this method. The object, shown in the upper-left panel, consists of two unresolved binaries, each with an angular separation of about $1/3$ of the diffraction limit λ/B , while the angular separation between the centres of the two stars is about $2/3$ of the diffraction limit. In each binary, the magnitude difference is zero, while the difference of magnitude between the two binaries is 0.5. The images have been generated by convolving the object with three ideal LBT PSFs, corresponding to equally spaced position angles (0° , 60° , and 120°) (see Anconelli et al., 2005b). For the first step, we selected 1000 OSEM iterations initialized with a uniform array; the result is shown in the upper-right panel of Fig. 15. The two binaries are resolved but not the individual components within the binaries. Then a mask has been estimated by selecting the pixels where the flux is greater than 50 % of the maximum value of the restored image; the result is shown in the lower-left panel. Finally this mask is used for re-initializing OSEM and the result is shown in the lower-right panel. The two binaries are clearly resolved. In this case the magnitudes are also obtained with sufficient accuracy (few percent errors) as well as the angular separations.

However, in our numerical simulations on binary systems we have verified that, when there is a significant difference of magnitude between the two stars, these may not be correctly estimated at the end of the second step, while their angular positions are, in general, correctly estimated. In order

to overcome this difficulty we propose the following third step.

Step 3 - Let us assume, in general, that the restored object, provided by Step 1 or Step 2, consists of q stars localized at the pixels P_1, P_2, \dots, P_q . We denote by $\mathbf{K}_j^{(i)}$ ($j = 1, \dots, p$) the PSFs centered at P_i and given by:

$$\mathbf{K}^{(i)} = \mathbf{K} * \delta(P_i) \quad , \quad (10)$$

where $\delta(P_i)$ is the characteristic function of the pixel, i. e. it is one at pixel P_i and zero elsewhere. Then we introduce the images:

$$\mathbf{g}_{j,c} = \sum_{i=1}^q c_i \mathbf{K}_j^{(i)} \quad , \quad (11)$$

depending on the unknown parameters $c = \{c_1, c_2, \dots, c_q\}$. These are determined by means of a least-squares method, namely by minimizing the discrepancy:

$$\Delta(c) = \sqrt{\sum_{j=1}^p \|\mathbf{g}_{j,c} - \mathbf{g}_j\|_2^2} \quad , \quad (12)$$

where $\|\cdot\|_2$ denotes the usual Euclidean norm.

In the example of Fig. 15 a pixel size of 1 mas is assumed. We have verified that, in principle, such an oversampling can be obtained by a suitable rebinning of LN images, so that the previous approach can be attempted on observed images.

As a result of several numerical simulations we have verified that, in the case of binaries with $\Delta m = 0$ and magnitudes from 10 to 17 in K-band, it is possible to reach an improvement of at least a factor of 4 with respect to the diffraction limit λ/B . On the other hand for binaries with an angular separation of $\lambda/2B$, it is possible to detect a difference of magnitude of the order of 4 in the brightest case and of the order of 2 in the faintest case. Detailed results are reported in Anconelli et al. (2005b).

15 Single-image approaches

In this Section, we summarize the results presented in Anconelli et al. (2005a) on single-image approaches to multiple-image deconvolution. Indeed, a possible approach to the solution of this problem is to look for methods combining the different images into a unique one containing all relevant information. At first glance, such an approach looks appealing: first because it becomes possible to use existing software for image deconvolution, and secondly, because the computational cost seems to be reduced. However, we recall that, for an algorithm such as OSEM, the cost of one iteration is just that of one single-image iteration of RLM.

There are many ways to combine the multi-images into a unique one. In this Section, we consider two of them. In both cases, we assume that if different images correspond to different integration times, $\tau_1, \tau_2, \dots, \tau_p$, then all images have been normalized, for instance, to the largest integration time τ_{\max} , i. e. \mathbf{g}_j has been multiplied by τ_{\max}/τ_j .

Method 1

The first approach is the most natural one and consists of a simple addition of the different images. In order to preserve normalization of the PSFs, it is convenient to take the arithmetic mean. Therefore

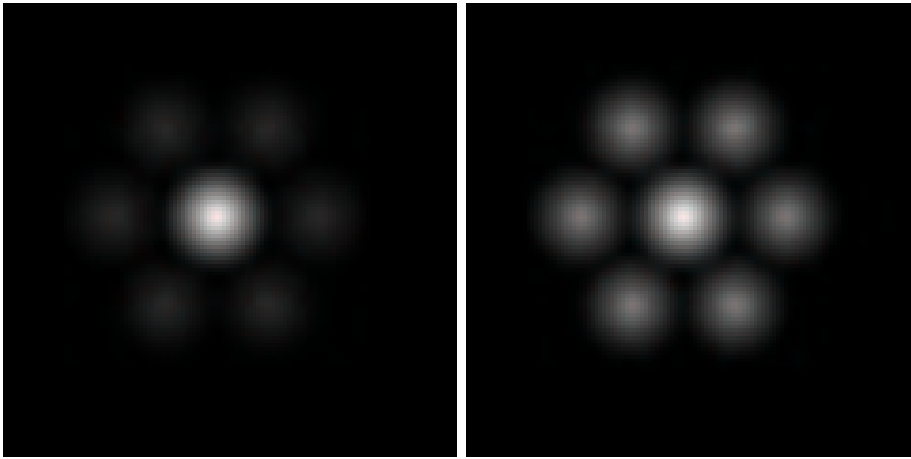


Figure 16: OTFs of the single-image approaches, corresponding to the ideal OTFs of Fig. 1: Method 1 in the left panel and Method 2 in the right panel.

the PSFs will be given by:

$$\mathbf{K}_{AV}(m, n) = \frac{1}{p} \sum_{j=1}^p \mathbf{K}_j(m, n), \quad (13)$$

with the corresponding image

$$\mathbf{g}_{AV}(m, n) = \frac{1}{p} \sum_{j=1}^p \mathbf{g}_j(m, n) . \quad (14)$$

The main features of this approach are the following:

- Both the PSF and the image are non-negative; moreover, the PSF is correctly normalized to 1 and the background of the image \mathbf{g}_{AV} is the arithmetic mean of the backgrounds of the images \mathbf{g}_j .
- If the images \mathbf{g}_j are corrupted by Poisson (photon) noise, then the average image \mathbf{g}_{AV} is also corrupted by Poisson noise since the sum of independent Poisson processes is also a Poisson process with an expected value given by the sum of the expected values.
- The addition of the images implies that in the domains of the u, v plane where only one image contains information, the effect of the others is just to add noise.

The left panel of Fig. 16 shows the OTF of the average PSF, \mathbf{K}_{AV} , in the case of the ideal PSFs of Fig. 1.

Method 2

In a recent paper Vio et al. (2004) propose a new method, derived from the least squares approach, for combining the multiple images into a single one. However, the relationship with the least-squares approach is not relevant and we consider here a different kind of combination which does not coincide exactly with that proposed by Vio et al. and has simpler properties.

The basic idea of the approach of Vio et al. is to define a transfer function which is obtained by taking, in a pixel m, n of the u, v plane, the value of the transfer function which has the maximum modulus, i. e.

$$\hat{\mathbf{K}}_{MM}(m, n) = \hat{\mathbf{K}}_J(m, n), \quad \text{if} \quad (15)$$

$$|\hat{\mathbf{K}}_J(m, n)| \geq |\hat{\mathbf{K}}_j(m, n)|, \quad \text{for } j = 1, \dots, p.$$

The OTF of this method is given in the right panel of Fig. 16, in the case of the ideal OTFs of Fig. 1. As it is obvious this procedure provides the correct contrast between the central disc and the side-discs, since these reproduce correctly those of the original OTFs.

Then we introduce the image which is quite naturally related to the transfer function defined in Eq. 15: it is defined by taking, in a pixel m, n of the u, v plane, just the value of the Fourier transform of the image with index J , i. e. that corresponding to the transfer function with the maximum modulus. We have:

$$\hat{\mathbf{g}}_{\text{MM}}(m, n) = \hat{\mathbf{g}}_J(m, n) . \quad (16)$$

The main features of this approach are the following:

- Both the PSF and the image, defined as the inverse Fourier transforms of Eqs. 15 and 16 respectively, may take negative values. These must be zeroed. Therefore, the PSF must be renormalized to guarantee that the sum of the pixel values is 1. Moreover, the total flux of the non-negative image must be computed and used in the RLM iterations. For simplicity, we do not change the notations of the PSF and of the image obtained with these operations from the original ones.
- The background of the image \mathbf{g}_{MM} will coincide with the largest background in the detected images, a difficulty in the case of very different observation times, so that the renormalization of the images mentioned at the beginning of this section is required.
- In the case of white noise affecting the images \mathbf{g}_j , the noise affecting the image \mathbf{g}_{MM} of Eq. 16 has a constant power spectrum.

If we apply RLM to the images of the two methods described above, it is obvious that the computational cost of one iteration is precisely that of one OSEM iteration, as defined in Eq. 6. Moreover, it is obvious that the same acceleration exponent can be applied in all cases. Therefore, the comparison between the efficiencies of the three methods simply consists in the comparison between the numbers of iterations required for reaching the optimal restorations. It is obvious that these optimal restorations, in general, do not coincide, so that their comparison provides insight into the accuracy of the three methods.

In our numerical experiments, we intend to compare the accuracy and efficiency of OSEM with that of the algorithms obtained by applying RLM to the images of *Method 1* and *Method 2*, denoted respectively as RL-AV and RL-MM. For this purpose, we consider three sets of PSFs, all corresponding to relative position angles of 0° , 60° and 120° . The first set consists of ideal PSFs, the second one of AO-corrected PSFs with different SRs for the three different orientations, and the third one of AO-corrected PSFs with the same SRs as before, but with the addition of the angular smearing effect.

The AO-correction effects are obtained again by an accurate model and simulation of the actual AO system aboard LBT by means of the software package CAOS. In order to take into account the anisoplanatic error, in addition to the other AO-correction errors (temporal error, WFS measurement error, DM fitting error etc.) we assume a two-layer turbulent atmosphere whose main physical parameters are: a mean velocity of 15 m/s, a wave-front outer-scale of 20 m, and values of the total Fried parameter of 12, 18, and 15 cm (at 500 nm), respectively for the PSF at 0° , 60° , and 120° ; these clearly correspond to three different observations during the night. As concerns the AO

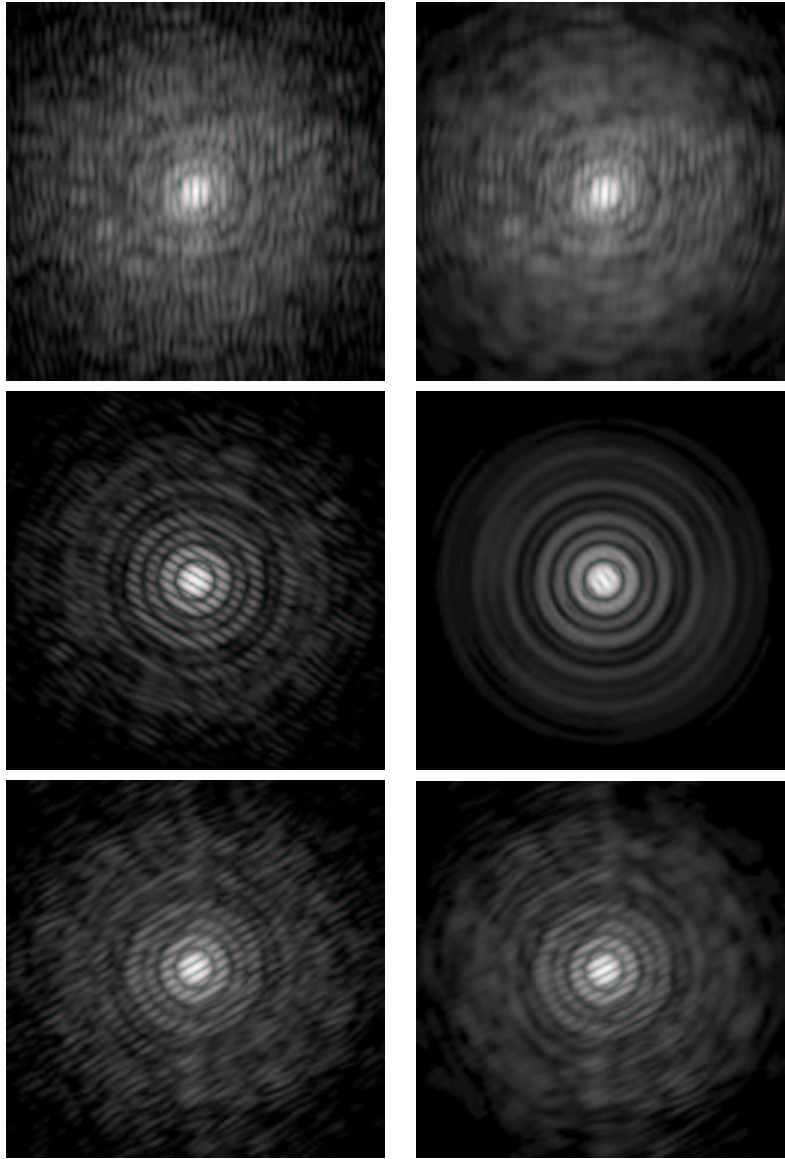


Figure 17: The AO-corrected PSFs used for the simulations described in Section 14 (logarithmic scale): PSFs without (left column) and with angular smearing effect (right column). These PSFs have been obtained with a total evolution time (atmospheric turbulence and AO system) of a few seconds.

	OS-EM		RL-AV		RL-MM	
	MV	SD	MV	SD	MV	SD
Minimum of the Restoration Error (RE)	4.8%	$\pm 0.1\%$	6.6%	$\pm 0.1\%$	6.2%	$\pm 0.1\%$
Optimal Number of Iterations	1536	± 141	705	± 40	366	± 13
Number of iterations providing $RE \leq 7\%$	168	± 6	385	± 56	149	± 6

Table 3: Comparison between the accuracy and efficiency of the three methods. We have used a 128x128 image of the diffuse object IRAS 04302+2247 with magnitude = 14, convolved with ideal PSFs and corrupted with 50 different realizations of noise; the reported mean values (MV) and standard deviations (SD) refer to these 50 realizations.

system itself, which is pyramid-based, the physical parameters are those foreseen for the system of LBT. We assume a configuration of 15×15 equivalent sub-apertures, a 13th magnitude guide star with optimized exposure time and number of LBT 672 mirror modes for each of the three different atmospheric conditions. The resulting SRs are 52% for the PSF at 0° , 87% for the PSF at 60° , and 79% for the PSF at 120° .

In the third set, the first and third PSFs are integrated over an angle of about 5° , while the second is integrated over an angle of about 45° ; in practice this angular smearing effect is obtained by adding snapshot PSFs for different orientations. The two sets of AO-corrected PSFs are shown in Fig. 17.

For the comparison of the three methods OSEM, RL-AV and RL-MM, we have used the accelerated algorithm with $\omega = 2$ and we have considered only one diffuse object, namely the YSO object IRAS 04302+2247 shown in Fig. 2, and the binary object shown in the same figure.

In a first set of experiments, we use a 128×128 image of the diffuse object, with magnitude 14, and we generate images by assuming ideal PSFs (corresponding to the three position angles indicated above), an integration time of 20 min, a sky background value of $12.5 \text{ mag}/''^2$ (K-band), a RON of $2 e^-$ rms, and a total transmission of 30%. For each image we generate, by means of AIRY, 50 noisy versions obtained with 50 different noise realizations (of Poisson type for the photon noise and of Gauss type for the RON). For each of these realizations we push the iterations of the three methods up to reach the minimum of the restoration error, as defined in Eq. 8. Then, for each method, we compute the mean value (MV) and the standard deviation (SD) of the 50 values of the minimum restoration error and of the corresponding number of iterations. The results are reported in the first two rows of Table 3.

As shown in the first row of Table 3, the most accurate restoration is provided by OS-EM, while the two single-image methods are approximately equivalent. In all cases, the standard deviation is quite small and that means that the minimum restoration error does not strongly depend on the noise realization. On the other hand, the second row shows that RL-MM is the most efficient method, with also a good stability of the number of iterations with respect to variations of the noise realization. OS-EM is the least efficient one with also a rather broad dispersion of the optimal number of iterations.

However, since the minimum of the restoration error is, in general, rather flat, we have considered the number of iterations required for reaching the same accuracy with the three methods. We have chosen a threshold of 7% since this accuracy can be reached by all the methods. The results are reported in the third row and we can conclude that, from this point of view, OS-EM and RL-MM are essentially equivalent.

In a second set of experiments we use three 256×256 versions of the same YSO object with different

magnitudes ($m = 14, 15$ and 16). For each value of the magnitude three sets of images are generated by convolving the object with the three sets of PSFs described above and adding the noise contributions (sky background, photon noise and RON). In these experiments, we consider only one noise realization, one for each set of PSFs. The purpose of these experiments is to compare the accuracy of the three methods and investigate its dependence on the magnitude of the object (hence on the SNR ratio) as well as on the AO-correction of the PSFs. The results are reported in Table 4 for the ideal PSFs, in Table 5 for the AO-corrected PSFs, and in Table 6 for the AO-corrected PSFs with the addition of the angular smearing effect. It follows that OS-EM always provides the best results even if the improvement of accuracy, with respect to the two other methods, does not strongly depend on the magnitude of the object and on the PSFs.

Magnitude	OS-EM % error	RL-AV % error	RL-MM % error
14	6.	7.3	7.2
15	7.9	10	9.3
16	9.8	11.4	12.6

Table 4: Comparison between the accuracies of the three methods in the case of the diffuse object with different magnitudes; images (256×256 pixels) have been convolved with ideal PSFs.

Magnitude	OS-EM % error	RL-AV % error	RL-MM % error
14	7.2	9.6	9.1
15	8.6	11.1	10.2
16	10	11.8	12.7

Table 5: Comparison between the accuracies of the three methods in the case of the diffuse object with different magnitudes; images (256×256 pixels) have been convolved with AO-corrected PSFs.

Magnitude	OS-EM % error	RL-AV % error	RL-MM % error
14	7.4	10.	8.7
15	8.6	11.2	9.6
16	10.2	12.8	11.6

Table 6: Comparison between the accuracies of the three methods in the case of the diffuse object with different magnitudes; images (256×256 pixels) have been convolved with AO-corrected PSF with angular smearing effect.

In a third set of experiments we consider the reconstruction of the binary system of Fig. 2. We have mainly investigated the case of two stars with the same magnitude ($m = 10$), by looking at the behaviour of the three methods for the three sets of PSFs. In Fig. 18 we give an example of the reconstructions we have obtained.

In the case of point objects the RL-like methods exhibit a convergent behaviour (instead of the semiconvergent one, which applies to the case of diffuse objects). This effect is shown in Figs. 19, 20, and 21, where we plot the reconstructed value of the flux of the binary as a function of the number of iterations for the three sets of PSFs we have considered.

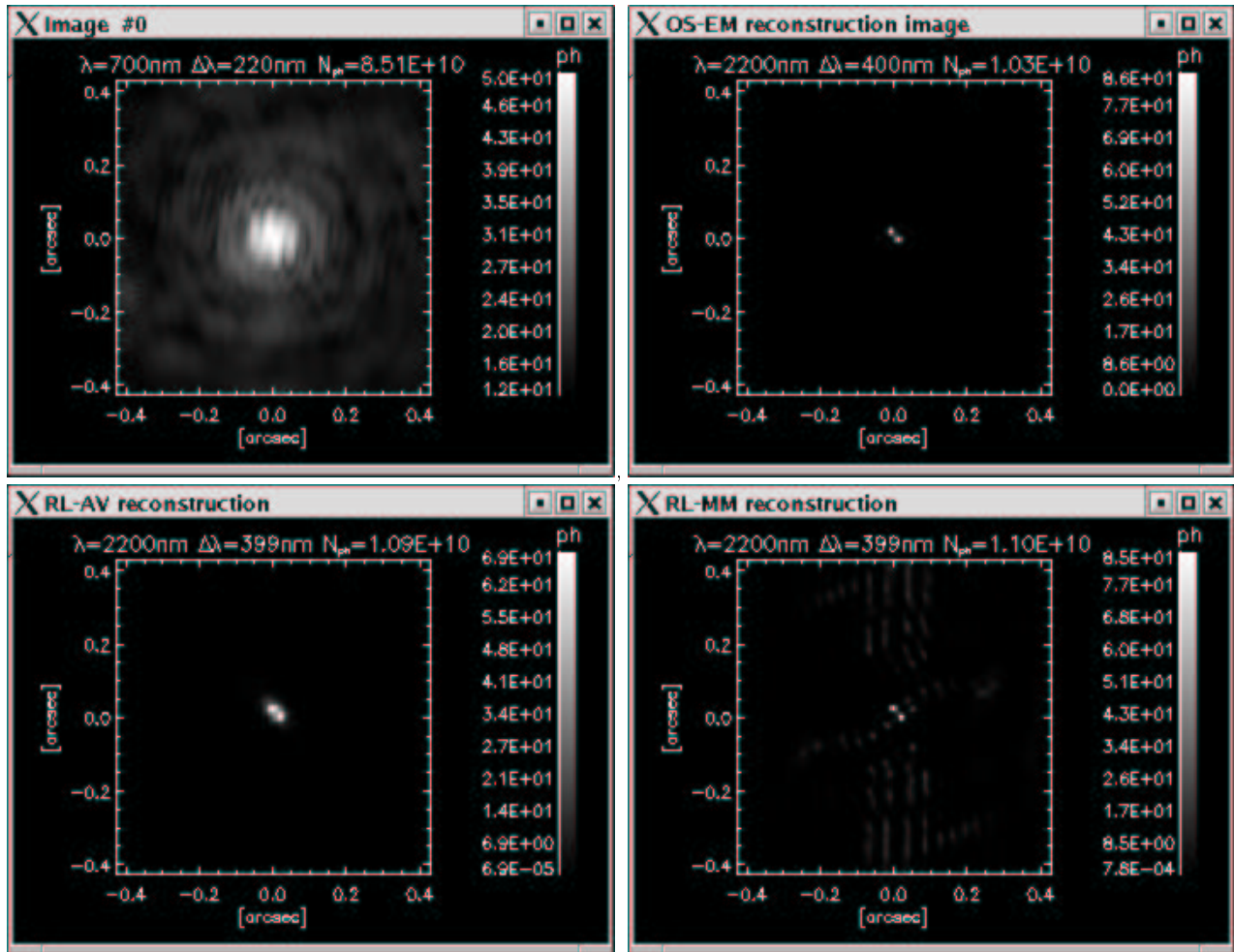


Figure 18: Example of reconstruction of the binary system with magnitudes 10. The images have been obtained by means of the AO-corrected PSFs with angular smearing effect. In the upper panels, one of the three images and the reconstruction provided by OS-EM are shown; in the lower panels, the reconstructions provided by RL-AV and RL-MM are displayed. The artifacts in the RL-MM reconstruction are probably due to the zeroing of the negative values in the MM-image.

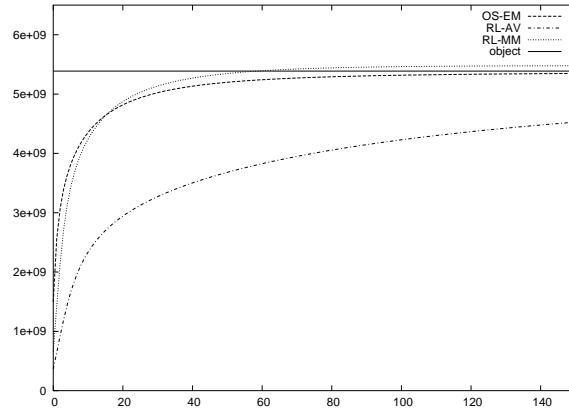


Figure 19: Behaviour of the flux of the binary object, with magnitude 10, as a function of the number of iterations: ideal PSFs.

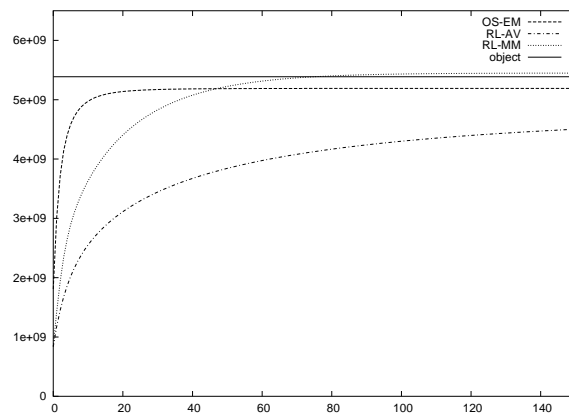


Figure 20: Behaviour of the flux of the binary object, with magnitude 10, as a function of the number of iterations: AO-corrected PSFs.

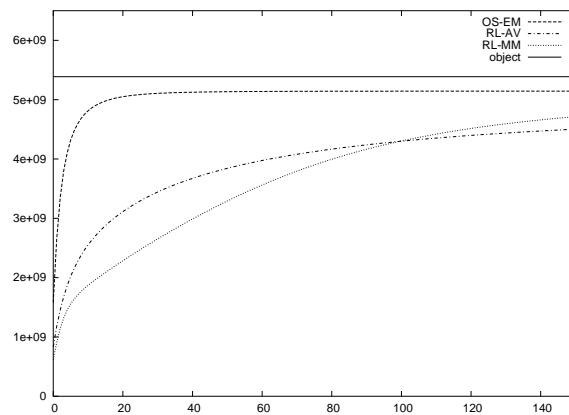


Figure 21: Behaviour of the flux of the binary object, with magnitude 10, as a function of the number of iterations: AO-corrected PSFs with angular smearing.

The comparison between OS-EM and RL-MM needs some discussion. As shown by the plots in the three panels, the OS-EM method always tends to underestimate the value of the flux while, in the first two cases, RL-MM provides a small over-estimate. This effect is due to the need of zeroing the negative values of the MM-image, given by Eq. 26, as we discussed in Section 4. As a consequence the total flux of the image is increased and this effect is at the origin of the over-estimation of the flux of the restored binary. In the third case (AO-corrected PSFs with angular smearing effect) OS-EM is definitely better than the two other methods.

16 Concluding remarks

Our numerical experiments, performed during the past three years, demonstrate that, in general, the resolution and imaging capabilities of LBT can be reached. We summarise the main features of our simulations:

- Mainly observations in K-band were considered.
- The pixel size is, in general, of the order of 6.7mas (three pixels within the resolution angle of 20mas), which is a bit larger than the actual pixel size of 5.12mas of the LINC-NIRVANA detector. Future simulations will be performed with the correct size. However the results reported in this document can only be improved by assuming a smaller pixel size.
- The magnitudes (or integrated magnitudes) of the objects we have considered range between 10 and 17. Moreover, we have assumed, in general, observation times of 20 minutes and a 30 % efficiency. These figures give an insight into the SNR of the images. We must also point out that we used a value of the RON of $2 e^-$ rms, which is probably a bit optimistic. However, a more realistic value should not modify significantly our results in the case of sky-background limited images.
- Binary stars can be resolved up to the diffraction limit, even with partial coverage, depending on the SR attained. With a good SR an improvement of resolution beyond the diffraction limit can be obtained by a rebinning of the data and a suitable initialization of OSEM.
- With a good SR, diffuse objects can be recovered also in the case of partial coverage.

As demonstrated by this document, CAOS and AIRY can be used to simulate a wide spectrum of observational situations and of scientific objects of interest to the astronomers. Moreover, for future simulations, CAOS could be replaced by LOST to simulate multi-conjugate AO. Therefore all these tools can be used for planning observations with LINC-NIRVANA.